

# Expectations of Physics beyond the Standard Model in ATLAS at the LHC

by

Jörgen Sjölin



Department of Physics  
Stockholm University  
2002



# Expectations of Physics beyond the Standard Model in ATLAS at the LHC

Akademisk avhandling

som för avläggande av filosofie  
doktorsexamen vid Stockholms Universitet  
offentligen försvaras i föreläsningshall FD5,  
Fysikum, Roslagstullsbacken 21,  
torsdagen den 30 maj 2002, klockan 10.00.

av

**Jörgen Sjölin**

## Abstract

The ATLAS detector at the CERN Large Hadron Collider will be a window to new unexplored energy domains in high energy physics. In this thesis the performance of the ATLAS hadronic calorimeter read-out electronics, jet reconstruction and sensitivity to possible extensions of the current Standard Model of particle physics are covered. Two possible extensions to the Standard Model are considered. One is gauge mediated supersymmetry breaking with the supersymmetric partner of the tau particle as the next-to-lightest supersymmetric particle, and the other is a general effective combined charge-parity violation in the top quark sector.

Fysikum  
Stockholms Universitet

Stockholm 2002  
ISBN 91-7265-472-4



# Expectations of Physics beyond the Standard Model in ATLAS at the LHC

by

Jörgen Sjölin



Department of Physics  
Stockholm University  
2002

Doctoral Dissertation 2002

Department of Physics  
Stockholm University  
Roslagnstullsbacken 21  
106 91 Stockholm  
Sweden

### **Abstract**

The ATLAS detector at the CERN Large Hadron Collider will be a window to new unexplored energy domains in high energy physics. In this thesis the performance of the ATLAS hadronic calorimeter read-out electronics, jet reconstruction and sensitivity to possible extensions of the current Standard Model of particle physics are covered. Two possible extensions to the Standard Model are considered. One is gauge mediated supersymmetry breaking with the supersymmetric partner of the tau particle as the next-to-lightest supersymmetric particle, and the other is a general effective combined charge-parity violation in the top quark sector.

# Contents

<b>1</b>	<b>Introduction</b>	<b>1</b>
1.1	The Standard Model . . . . .	2
1.2	Beyond the Standard Model . . . . .	2
<b>2</b>	<b>Theory and issues of model building</b>	<b>4</b>
2.1	Symmetries . . . . .	4
2.2	An enlightening example . . . . .	5
2.3	Standard Model basics . . . . .	5
2.4	Higher order corrections and renormalization . . . . .	7
2.5	From model to observables by the $S$ -matrix . . . . .	8
<b>3</b>	<b>The LHC</b>	<b>10</b>
<b>4</b>	<b>The ATLAS detector</b>	<b>11</b>
4.1	The inner detector . . . . .	12
4.2	Calorimetry . . . . .	12
4.3	The muon system . . . . .	13
4.4	The trigger . . . . .	13
<b>5</b>	<b>Hadronic calorimetry</b>	<b>15</b>
5.1	The Tile calorimeter . . . . .	16
5.2	Detector calibration and monitoring . . . . .	18
5.2.1	Detector and PMT response via cesium 137 . . . . .	19
5.2.2	Laser surveillance of the PMT stability . . . . .	19
5.2.3	Electronics calibration via charge injection . . . . .	19
5.3	Fast readout electronics requirements . . . . .	21
<b>6</b>	<b>Jets in the ATLAS detector</b>	<b>23</b>
6.1	Jet reconstruction . . . . .	24
6.2	Results . . . . .	28
<b>7</b>	<b>Signatures of supersymmetry</b>	<b>30</b>
7.1	Supersymmetry breaking . . . . .	31
7.2	$\tilde{\tau}$ as the NLSP in ATLAS . . . . .	32
7.2.1	The model . . . . .	33
7.2.2	Analysis . . . . .	33
7.2.3	Results . . . . .	34
<b>8</b>	<b><math>CP</math> violation beyond the Standard Model</b>	<b>36</b>
8.1	Effective theory of $CP$ violation in $t\bar{t}$ production . . . . .	36
8.2	ATLAS sensitivity to an anomalous $g t \bar{t}$ vertex . . . . .	39
8.2.1	Event production . . . . .	39
8.2.2	Analysis . . . . .	40
8.2.3	Results . . . . .	42

<b>9 TileCal test-beam</b>	<b>43</b>
9.1 Charge reconstruction . . . . .	44
9.1.1 Pulse shape reconstruction . . . . .	45
9.1.2 Readout linearization . . . . .	45
9.2 The concept of non linear compression, test-beam 1994 . . . . .	46
9.3 A comparative test of non linear compression, test-beam 1995 . . . . .	46
9.4 Approaching realistic ATLAS requirements, test-beam 1996 . . . . .	48
9.4.1 Pedestal analysis . . . . .	48
9.4.2 Pulse shape invariance . . . . .	49
9.4.3 Charge estimator resolution . . . . .	53
9.5 Second iteration and the bigain backup solution, test-beam 1997 . . .	58
9.5.1 Compressor: pulse shape invariance . . . . .	58
9.5.2 Compressor: charge estimator resolution . . . . .	61
9.5.3 Bigain: pulse shape invariance and resolution . . . . .	63
9.5.4 Global correlations . . . . .	64
9.6 10 bit or 12 bit ADC for bigain compression, test-beam 1998 . . . . .	64
9.6.1 Pedestal analysis . . . . .	65
9.6.2 10 bits or 12 bits ADCs in the final design . . . . .	67
<b>10 Conclusions and outlook</b>	<b>68</b>
<b>A Conventions and definitions</b>	<b>70</b>
A.1 Units . . . . .	70
A.2 Special relativity . . . . .	70
A.3 The Dirac field . . . . .	71
A.4 Gauge connections . . . . .	72
A.5 Lie groups . . . . .	72

## Accompanying papers

- I. **Jet reconstruction in the ATLAS barrel calorimeter,**  
J. Sjölin,  
ATL-TILECAL-2000-009.
- II. **A study of Gauge Mediated Supersymmetry Breaking with  $\tilde{\tau}$  as the NLSP in the ATLAS detector,**  
J. Sjölin,  
SN-ATL-2001-004, to appear in the European Physics Journal.
- III. **TOPSPIN - A Monte Carlo generator for  $t\bar{t}$  events with anomalous  $g t\bar{t}$  couplings,**  
J. Sjölin,  
ATL-PHYS-2002-011.
- IV. **LHC experimental sensitivity to  $CP$  violating  $g t\bar{t}$  couplings,**  
J. Sjölin,  
ATL-PHYS-2002-012.
- V. **Studies of internal resolution for 12bit and 10 bit ADCs in the Tile-Cal read-out electronics,**  
S.O. Holmgren and J. Sjölin,  
ATL-TILECAL-98-135.



# 1 Introduction

Particle physics is about the fundamental interactions among the smallest constituents that make up our universe. The development of the current understanding is both an amazing and intriguing series of interplay between experimental discoveries and theoretical insights. Over the years, many people have contributed important pieces to this understanding. But what does it mean to understand something so abstract as point particles that you cannot even see? If you think about it, you “understand” something by building a model that is able to predict your observations. The model encodes the rules and principles that you learned or that you suspect your observations always follow. There will also be properties that you don’t understand. This lack of understanding is hidden behind a set of parameters in your model. The goal is of course to reduce the number of parameters, or at least make sure that the numbers you got parameterize all your existing data.

As soon as you find that your model predictions deviate from your observations, by say more than five standard deviations, you know that there is something that you do not understand. First you check that there are no systematic errors in the data that you have not accounted for. Then you must make sure that the circumstances for the observation is within the validity domain of the model. This is a very important point. For example, we still use Ohm’s law in most circuit calculations even if we know that Maxwell’s equations give a much more fundamental description. Maxwell’s equations on the other hand are used when Quantum Electro Dynamics (QED) is known to give more exact results by many orders of magnitude. The reason for not using QED when you for example estimate the dimension of the cable for the light bulb in your kitchen, is that the details correctly modeled by QED (i.e. the quantum fluctuations) are irrelevant at the energy scale of the processes involved. The approximation is valid because there are degrees of freedom that do not contribute at low energies. However, at higher energies these degrees of freedom become active and may actually dominate the whole process. The systematic treatment of a model where some of the degrees of freedom are integrated out is called an effective theory. Until we have an ultimate theory of everything one can argue that all theories are effective theories. And as we probe deeper and deeper into the void of unexplored energy territories, new degrees of freedom are expected to pop out and surprise us.

The best description we have today of the experimental data at the highest achievable energies is the Standard Model (SM) [1]. It is a quantum field theory, that is the matter content is described by fields at every point in space-time. The huge success of the SM is that all the interactions are given by a few very simple symmetry assumptions of these fields, and most importantly, it enables calculations of the outcome of all observations to arbitrary precision. That this is indeed the case has been proved rigorously by t’Hooft and Veltman, for this they got the Nobel prize in 1999. At that time the two most powerful microscopes in the world, the LEPIII accelerator at CERN, and the Tevatron accelerator at Fermilab had verified many vital aspects of the predictions of the SM.

## 1.1 The Standard Model

The lesson we have learned from the last century is that symmetries have a fundamental role to play in our description of the laws of the universe. Emmy Noether pointed out for us that for every symmetry there is an associated conserved current. For example, the conservation of energy can be viewed as a consequence of invariance under time translations. This idea can be driven surprisingly far. We notice to begin with that the electric charge is conserved. Hence, we automatically suspect that there is a symmetry lurking behind the scenery. This symmetry turns out to be a symmetry under local rephasing of the field carrying electric charge. Symmetries can be described in terms of something called a group, and the unitary rephasing of a complex field is classified as a  $U(1)$  symmetry. If we now turn the arguments around and start with the  $U(1)$  local symmetry and see what happens to our model description something beautiful happens. Given the charged matter field and the  $U(1)$  symmetry the photon automatically appears as a requirement to maintain the local  $U(1)$  symmetry, or in the jargon often used, maintain the gauge invariance. The photon is responsible for the electromagnetic force. The natural question is then: can all forces be described in terms of local symmetry assumptions? The answer seems to be yes, they can! Particle physics deals with the electromagnetic, the weak and the strong force. And they are all understood in terms of the combined local symmetry:  $SU(3)_c \times SU(2)_L \times U(1)_Y$ . So much about the interactions, what about the matter contents? All matter that we see around us consists of fermions, i.e. they obey Fermi-Dirac statistics and carry half-integer spin, and for each matter field there is a corresponding anti-matter field. It is important to understand that the matter fields in the SM are massless, otherwise it is impossible to achieve gauge invariance.

The central part of the SM is the breaking of the  $SU(2)_L \times U(1)_Y$  symmetry down to  $U(1)_{em}$ . This is done by adding a complex scalar field doublet to the model, called the Higgs field, with a potential that triggers spontaneous symmetry breaking. The electro-weak symmetry breaking generates the mass of the  $W$  and  $Z$  bosons and also enables the fermions to acquire mass while still preserving the gauge invariance. All predictions associated with the SM electroweak symmetry breaking have been confirmed experimentally, including very sensitive higher order loop corrections. Remember that the number of parameters was an indication of how much we still don't understand. The SM contains 19 parameters: the fermion couplings(9) to the scalar field, the gauge couplings(3), the CKM matrix(4) that relates the quark weak eigenstates with the mass eigenstates in charged weak currents, the QCD phase  $\Theta$  associated with the strong  $CP$  problem(1), the vacuum expectation value(1) and the Higgs self coupling(1). Of all these parameters only the Higgs self coupling remains unknown.

## 1.2 Beyond the Standard Model

The SM is overwhelmingly successful. Since the SM represents our current understanding of particle physics it is natural to ask: where do we go from here? There

is no significant direct evidence that the SM is wrong, but there are some “smoking guns” that do not fit well into this picture

- In the SM neutrinos are massless. However, the Super-Kamiokande experiment [2] has strong evidence that can be interpreted as neutrino oscillations. Oscillations are due to mass differences and hence neutrinos are likely to have mass.
- The couplings of the forces “run”, i.e. they evolve according to well determined renormalization group equations (RGE). There are ideas that if the SM is an effective theory of some Grand Unified Theory (GUT) with higher symmetries, then the couplings should unify at some high energy scale, the GUT scale. However, if the RGE’s of the SM are extrapolated to high energies they fail to unify at any scale.
- The strong  $CP$  parameter  $\Theta$  [3] is limited to an extremely small value by measurements of the neutron electric dipole moment [4]. This is highly unnatural given the level of  $CP$  violation in the electro-weak sector.
- The SM relies on the Higgs mechanism. Where is the Higgs particle, and how is it stabilized from quadratic divergences? Maybe there is no Higgs particle and maybe electro-weak symmetry breaking is triggered by some other mechanism, for example Technicolor.

The list is not exhaustive. There are many fundamental questions: how does gravity fit in to the picture, why are there three families of fermions, and so on. These questions will need experimental input before we can improve our understanding.

This thesis will give an overview of an instrument that has the potential to answer many of these questions. It is still under construction and will remain so for many years to come. You will notice that the emphasis will be on the hadronic calorimetry and the associated jet reconstruction. This is due to the fact that the author has been active in the evaluation of the fast read-out electronics of the hadronic calorimeter, and participated in the analysis of the expected performance of the jet reconstruction. But, as you will see later on in the accompanying papers with examples of analysis of simulated beyond SM physics, jets will be very important. Two extremely important sectors will be exemplified which both regard the breaking of symmetries. That it happens to be all about violation of symmetries is not a random coincidence, but that you probably understand by now.

## 2 Theory and issues of model building

The language used for the modeling and understanding of particle physics is quantum field theory (QFT). The ingredients absolutely necessary to describe high energy elementary particles are quantum mechanics (QM) and special relativity (SR). When QM and SR are active at the same time it is an experimental fact that the processes involved cannot be described by a fixed number of single particles. A better description is given by a field that is able to annihilate and create particles out of the vacuum. The successful environment where QM, SR and the concept of fields can coexist is QFT. In a QFT, the fundamental recipe is the Lagrangian ( $\mathcal{L}$ ), or more precisely the Lagrangian density, a real valued scalar. The Lagrangian reflects all the properties of the model. Any measurable quantity that is accurately modeled has its origin in the Lagrangian. In particular this is true for symmetries.

### 2.1 Symmetries

Symmetries come in two flavors, continuous and discrete symmetries. The most interesting continuous symmetries can be classified into something called Lie groups, see Appendix A.5. The Poincaré Lie group, which is the Lorentz group and the group of translations in space-time, contains the fundamental symmetries we expect from any sensible model. For example, the description of physical processes is time independent. From this symmetry, via Noeters theorem, follows that energy is conserved. Continuous symmetries also form the basis for the SM, where the symmetries act among the fields themselves in an abstract symmetry space. The general treatment of these internal symmetries is perhaps one of the most important steps in the development of QFT. It is known as Yang-Mills theory.

Examples of discrete symmetries are: charge conjugation ( $C$ ), parity ( $P$ ), that is  $x$  is replaced by  $-x$ , and time reversal ( $T$ ). One of the things that have been proved rigorously in QFT is that given Lorentz invariance and positive energy states, one finds that the combined symmetry  $CPT$  is automatically conserved. This is known as the  $CPT$ -theorem [5]. That  $CPT$  indeed is a good symmetry has been demonstrated in the neutral kaon system to a precision of  $10^{-18}$ . What about the  $CP$  symmetry? Given just two lepton families it turns out to be impossible to accommodate  $CP$  violation within the framework of the SM. Yet, in 1964 Cronin and his collaborators [6] found that the  $CP$  symmetry was violated in the neutral kaon system at the  $10^{-3}$  level. This came as a total surprise, and it was not until 1973 that finally Kobayashi and Maskawa showed that  $CP$  naturally could be incorporated into the SM if there were 3 lepton families. There were other proposals with beyond the standard model explanations, like Wolfenstein's Superweak model [7], but the presence of  $CP$  violation in the B-meson system verified by the BaBar [8] and Belle [9] experiments strongly favors the SM explanation.

## 2.2 An enlightening example

To shed some light on how the QFT Lagrangian machinery works and how the connection with symmetries is manifest, let's have a look at perhaps the best example there is. Electric charge is conserved, and we know by now that this can be modeled by imposing  $U(1)$  local symmetry of the field that describes the electron. The electron is described by a field ( $\psi$ ) that satisfies the Dirac equation. At this point the reader is referred to Appendix A for an overview of the definitions in QFT and the conventions used in this thesis. Now we can ask: what is the most general Lagrangian that we can write down assuming Lorentz invariance and  $U(1)$  symmetry that has mass dimension 4<sup>1</sup> or less? The answer is (see reference [10])

$$\mathcal{L} = \bar{\psi}(i\gamma^\mu D_\mu)\psi - \frac{1}{4}F^{\mu\nu}F_{\mu\nu} - c\epsilon^{\alpha\beta\mu\nu}F_{\alpha\beta}F_{\mu\nu} - m\bar{\psi}\psi.$$

At this point one begins to understand the power of symmetries. The symmetries, when expressed in this convenient notation, restrict the Lagrangian to just a handful of terms. Let's take a closer look at the individual quantities. The first term is the kinetic term of the electron. The covariant derivate  $D_\mu$  is the replacement of the normal derivative which must be used in order to maintain the  $U(1)$  local symmetry and it is given by

$$D_\mu = \partial_\mu + ieA_\mu.$$

Here the photon gauge field  $A_\mu$  appears due to the symmetry requirements, and  $e$  is the electric charge that acts as a gauge coupling of the photon field. When we expand the covariant derivative in the Lagrangian, we find the term responsible for the interaction of the electron with the photon field. This is the origin of the statement of interactions by symmetries. The next term is comprised of pure gauge fields where  $F_{\mu\nu}$  is called the electromagnetic field tensor and it is given by

$$ieF_{\mu\nu} = [D_\mu, D_\nu].$$

The third term violates the discrete  $CP$  symmetry, and since  $CP$  is a good symmetry in electromagnetic interactions the coupling constant  $c$  must be zero or very small. Quite generally one can say that if a term is allowed it will be present unless there is a symmetry that forbids it. In this case we just impose the  $CP$  symmetry from our observations. The last term is a mass term for the electron. What is left of this model is nothing else but QED. QED is experimentally verified to a precision of  $10^{-12}$ , the best verified physical theory by many orders of magnitude. The classical limit of the equations of motion given by  $\mathcal{L}$  are the Maxwell's equations.

## 2.3 Standard Model basics

Before we look for beyond the SM physics, we better have a clear notion of what the basic properties of the SM are. In the SM each quark and lepton, that is every

---

<sup>1</sup>The reason for mass dimension 4 has to do with renormalizability, and it means that the predictions are free of divergences to all orders in perturbation theory.

elementary matter particle, is represented by a fermionic field in a definite left or right helicity state. This is possible since the fields are massless. A mass term is strictly forbidden since it would mix left and right helicity and break the imposed gauge symmetries. Each matter field belong to a left doublet and a right singlet representation under  $SU(2)$ , except for the neutrinos which we in the SM assume to exist only in the left representation. The quark matter fields are

$$q_L^i = \left[ \begin{pmatrix} u_L \\ d_L \end{pmatrix}, \begin{pmatrix} s_L \\ c_L \end{pmatrix}, \begin{pmatrix} t_L \\ b_L \end{pmatrix} \right], \quad u_R^i = [u_R, s_R, t_R], \quad d_R^i = [d_R, c_R, b_R],$$

and the lepton matter fields are

$$l_L^i = \left[ \begin{pmatrix} \nu_e \\ e_L \end{pmatrix}, \begin{pmatrix} \nu_\mu \\ \mu_L \end{pmatrix}, \begin{pmatrix} \nu_\tau \\ \tau_L \end{pmatrix} \right], \quad l_R^i = [e_R, \mu_R, \tau_R].$$

The fields carry spin indices that will be suppressed unless needed, and the quark fields implicitly also carry color charge indices (e.g. color = red, green and blue). The Lagrangian of the SM is required to respect the symmetries  $U(1)$  of weak hypercharge ( $Y$ ),  $SU(2)$  of the left helicity fields, and  $SU(3)$  of colors of the quark fields. Once this is done the interactions of the model is fixed. For each generator of the gauge group there is an associated gauge field, and the complete covariant derivative reads

$$D_\mu = \partial_\mu + ig' B_\mu Y + ig W_\mu^i \tau^i + ig_s G_\mu^i T^i,$$

where  $Y$  is the  $U(1)$  generator,  $\tau^i$  are the three generators of  $SU(2)$  and  $T^i$  are the eight generators of  $SU(3)$ . The  $g'$  and  $g$  couplings are the electro weak couplings which are related by a unitary rotation by the Weinberg angle in order to give the correct electromagnetic behavior, and  $g_s$  is the strong coupling constant. The  $G_\mu^i$  are the eight gluon fields, and  $B_\mu$  and  $W_\mu^i$  are the electro-weak fields. This all looks very promising, except that all fields are massless and there is no room for  $CP$  violation in the quark sector. This is in wide contrast with experiments. One solution is to add a massless complex scalar  $SU(2)$  doublet field to the model, with a potential that triggers spontaneous symmetry breaking (SSB). SSB means that there exist ground states that locally violate the symmetry of the full Lagrangian. In the SM one assumes the potential

$$V(\Phi^\dagger \Phi) = \mu^2 \Phi^\dagger \Phi + \lambda (\Phi^\dagger \Phi)^2, \quad <\Phi>_0 = \begin{pmatrix} 0 \\ v/\sqrt{2} \end{pmatrix}, \quad v = \sqrt{-\frac{\mu^2}{\lambda}}.$$

The vacuum expectation value (VEV)  $v$ , of the scalar Higgs field is measured indirectly to be

$$v = (\sqrt{2}G_F)^{-1/2} = 246 \text{ GeV},$$

where  $G_F$  is the Fermi constant. However, the mass ( $\sqrt{-2\mu^2}$ ) and the self coupling ( $\lambda$ ) remain unknown. When the covariant derivative in the scalar piece of the SM Lagrangian

$$\mathcal{L}_S = D_\mu \Phi^\dagger D^\mu \Phi - V(\Phi^\dagger \Phi)$$

is expanded after the SSB, two degrees of freedom of the Higgs field are absorbed by two of the gauge fields as they become massive, one degree of freedom is gauged by the  $U(1)$  symmetry, leaving just one real massive scalar. This is in perfect agreement with experiments and one of the triumphs of the SM.

The Higgs field also offers a gauge invariant way to generate mass to the fermions. The Lagrangian for the quark masses is

$$\mathcal{L}_{Yq} = -G_u^{ij}\bar{u}_R^i\tilde{\Phi}^\dagger q_L^j - G_d^{ij}\bar{d}_R^i\Phi^\dagger q_L^j + h.c., \quad \tilde{\Phi} = i\sigma_2\Phi^*,$$

which implies the mass matrix

$$M^{ij} = \frac{v}{\sqrt{2}}G^{ij}.$$

There are some profound consequences given by the form of the quark mass Lagrangian. If the fields that make up the mass eigenstates are a mixture of weak eigenstates, one finds that  $\mathcal{L}_{Yq}$  prevents a redefinition of the fields such that they can become the same in both pictures. This implies physical and measurable consequences in the electro-weak sector if we work in the mass basis. The relation between the pictures is given by unitary rotations  $u'^i = U^{ij}u^j$  and  $d'^i = D^{ij}d^j$ . Since  $U^\dagger U = 1$  there will be no mixing of the states in neutral electro-weak currents<sup>2</sup>, that is no flavor-changing neutral current (FCNC). For charged currents on the other hand, there is a transition between up-type and down-type quarks which results in a matrix

$$\text{CKM} = U^\dagger D.$$

This is the famous matrix first discussed by Kobayashi and Maskawa [12]. It can be parametrized in terms of three Euler rotations and one phase. The fact that one phase remains after redefinitions of the fields means that this is a possible source of  $CP$  violation. Experiments also suggest that this is indeed the preferred way to describe the  $CP$  violating processes we have yet observed in the laboratory.

Notice that there is no CKM matrix for the leptons, and hence no room for  $CP$  violation in the lepton sector. The reason is that there are no  $\nu_R$  fields, and thus the less restrictive lepton Lagrangian permits a redefinition of the lepton fields such that the mass and electro-weak eigenstates are the same. If we would include the results from the Super-Kamiokande experiment and insist that neutrinos have mass, this would no longer be the case.

## 2.4 Higher order corrections and renormalization

The parameters that enter in the free Lagrangian are not the parameters that we will observe when the interactions are included. The reason is that there are quantum fluctuations that introduce corrections to the bare parameters. Examples of such parameters are the electron mass and the coupling constants. Then how can we do

---

<sup>2</sup>This also happens for just two families, where the rotation is described by the Cabibbo angle. The cancellation is called the GIM mechanism [11].

any reliable calculations at all if we do not know the true values of the Lagrangian? The answer is renormalizability. If the theory is renormalizable, we can calculate the physical parameters up to say one loop from the bare parameters using a momentum cut-off  $\Lambda$ , calculate the field rescaling, solve the expression for the physical parameters and in the end let  $\Lambda \rightarrow \infty$ . This means that we can renormalize our Lagrangian such that the parameters that appear are the physical parameters plus some well defined counter terms. One way of looking at it is that we have defined a new theory at the renormalization scale and absorbed all the higher order details into the measured parameters and the renormalization conditions. The parameters will in general depend both on the renormalization scale and on the momentum. The dependence of the parameter on the momentum is called running and is determined by the renormalization group equations (RGE).

All the Lagrangians we have encountered so far are classical. In order to quantize, the unphysical degrees of freedom must be removed by gauge fixing terms in the Lagrangian. The physics of the end result does not depend on the gauge choice, but the gauge can have a huge impact on the complexity of the calculations. Once the theory is quantized it may break the symmetries of the classical Lagrangian by quantum effects. This is called anomalies. If the theory contains anomalies it will not be renormalizable. Maybe one of the strongest properties of the SM is that it is anomaly free. In an almost magical coincidence, the property of complete families of the SM renders it free of anomalies.

## 2.5 From model to observables by the $S$ -matrix

In order to be predictive, it must be possible to calculate decay rates and scattering cross-sections. For most of the cases it does not exist an exact expression that takes us from the Lagrangian to the observables. However, as long as the interactions can be regarded as perturbations to the free Lagrangian the result can be expressed as a perturbation series. The perturbations can be ordered in a well defined and compact set of rules, called the Feynman rules. These rules, which are mathematical entities, can be visualized in an intuitive way as single particle point interactions (vertices) and correlations between points in space-time (propagators) called Feynman diagrams. A scattering process can be regarded as a transition amplitude between the input states  $|k_1 k_2\rangle_{\text{in}}$  and the output states  ${}_{\text{out}}\langle p_1 p_2|$ . The amplitude can be rewritten as

$${}_{\text{out}}\langle p_1 p_2|k_1 k_2\rangle_{\text{in}} = {}_{\text{out}}\langle p_1 p_2|S|k_1 k_2\rangle,$$

where  $S$  is called the S-matrix, a unitary operator that relates the the input states at the infinite past to the output states at the infinite future. Since  $S = 1$  for the case of no interactions we can extract the interesting part by

$$S = e^{iT} \simeq 1 + iT.$$

The scattering part is thus contained in  $iT$ . In order to make four-momentum conservation manifest  $T$  is redefined into a matrix element  $\mathcal{M}$  defined by

$${}_{\text{out}}\langle p_1 p_2|iT|k_1 k_2\rangle = (2\pi)\delta^4(P - \sum_i p_i)i\mathcal{M},$$

where  $P = p_1 + p_2$ . The differential decay rate of a particle of mass  $M$  is now given by [75]

$$d\Gamma = \frac{|\mathcal{M}|^2}{2M} d\Phi_f,$$

where  $d\Phi_f$  is the phase-space factor given by

$$d\Phi_f = (2\pi)^4 \delta^4(P - \sum_i^n p_i) \prod_i^n \frac{d^3 p_i}{(2\pi)^3 2E_i}.$$

The differential cross-section of a two body collision between particles of masses  $m_1$  and  $m_2$  is given by [75]

$$d\sigma = \frac{|\mathcal{M}|^2}{4\sqrt{(p_1 p_2)^2 - m_1^2 m_2^2}} d\Phi_f$$

The actual calculation of  $\mathcal{M}$  is in principle not harder than following a cookbook recipe. The recipe says

$$i\mathcal{M} = \text{sum of all connected, amputated Feynman diagrams.}$$

Connected means that all points should be connected, and amputated means that the propagator of the external legs of each diagram should not contain other diagrams. Since the Feynman rules are part of the perturbation expansion of the interactions, one can directly read off the Feynman vertices from the interaction terms in the Lagrangian by multiplying by a factor of  $i$  and a symmetry factor. For a detailed description of the  $S$ -matrix and the construction of Feynman diagrams see reference [10].

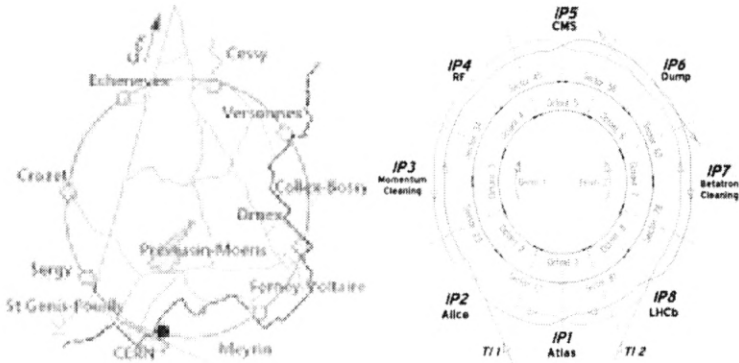


Figure 1: The geographical location of the LHC tunnel (left), the different experiments are also shown (right).

### 3 The LHC

To challenge the SM and reach physics at energies 10 times higher than the current limits, a new 14 TeV center-of-mass energy proton-proton collider is being built at CERN (European Organization for Nuclear Research) in Geneva. It will be ready for operation in 2007. Today our current state-of-the-art knowledge comes from LEP, the 200+ GeV electron-positron collider which will be replaced by the Large Hadron Collider (LHC), and the Tevatron, the 1.8 TeV proton-antiproton collider at Fermilab. With LHC particles with masses in the TeV range can be produced. Hence LHC will be able to either falsify or confirm supersymmetry or the existence of any SM model Higgs particle. LHC will also be able to accelerate heavy ions instead of protons to study quark-gluon phase transitions at high energy densities.

LHC will replace LEP and use the same 27 km long tunnel, see Figure 1. The 7 TeV beam and the fixed radius define a peak magnetic dipole field of 8.3 T. A lot of technical development was required to enable the superconducting magnets needed for this large field to operate reliably at 1.9K. The amount of material that has to be cooled is 31,000 tons. The inner diameter of the magnets is 56 mm, and the two beams are separated by 194 mm. After filling, the protons are accelerated from 450 GeV to 7 TeV and the luminosity  $\mathcal{L} = 10^{34} \text{ cm}^2\text{s}^{-1}$  is maintained for 10 hours before a new filling is needed.

In order to study the particles created in the collisions, huge and highly advanced detectors will be placed around the four interaction points. Under construction are two general purpose detectors ATLAS and CMS, one detector ALICE for heavy ion collisions and one detector LHC-B for B-physics, see Figure 1.

For the first three years LHC is expected to run at low luminosity  $\mathcal{L} = 10^{33} \text{ cm}^2\text{s}^{-1}$ , accumulating  $10 \text{ fb}^{-1}$  per year per experiment, then continue to run at full luminosity  $\mathcal{L} = 10^{34} \text{ cm}^2\text{s}^{-1}$ , accumulating  $100 \text{ fb}^{-1}$  per year per experiment.

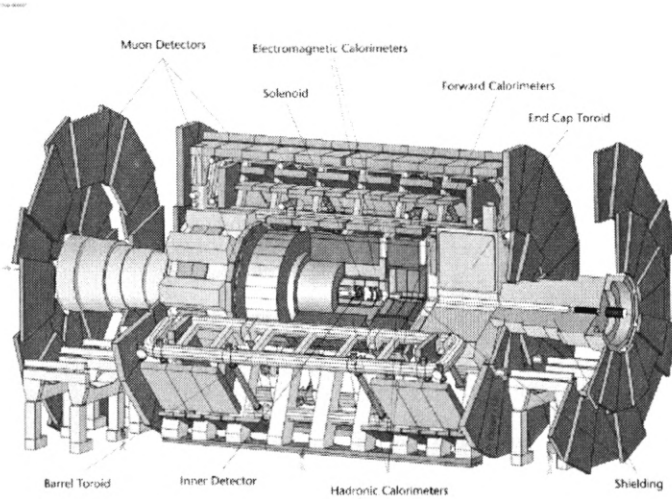


Figure 2: Overview of the ATLAS detector.

## 4 The ATLAS detector

ATLAS [24] is one of two general purpose detectors utilizing the LHC. It is designed to cover as much as possible of the physics that can be generated in the 14 TeV proton-proton collisions, see Figure 2. Most of the particle detectors in collider experiments have the same overall cylindrical configuration. Starting from the interaction point there are the following detectors: a tracker to reconstruct charged tracks in a magnetic field, an electromagnetic calorimeter, a hadron calorimeter and a muon spectrometer. The general design is aiming for:

- Good solid angle coverage. This is measured in the boost invariant parameters  $|\eta| < 4.9$  and  $\phi \simeq [0, 2\pi]$ . The pseudorapidity,  $\eta$ , is defined as  $-\ln \tan \theta/2$ , where  $\theta$  is the polar angle from the beam axis, and  $\phi$  is the azimuthal angle. A hermetic coverage is needed among other things for good missing energy resolution, which is heavily used e.g. in supersymmetry searches.
- Excellent electromagnetic calorimetry for electron/photon separation and accurate electron, photon and jet measurements to very high energies. Accurate jet measurements also require a thick and hermetic hadron calorimeter to avoid false missing energy.
- Powerful tracker that in a robust way can handle high track multiplicities, resolve charged particles with high transverse momentum ( $p_T$ ) and tag  $\tau$  and heavy flavor quarks.

- High energy resolution of muons at high rates. This is solved by a large independent external muon system.
- Fast and sensitive trigger to enable effective filtering of interesting physics in a tremendous background of 23 interactions per bunch crossing at a rate of 40 MHz.

## 4.1 The inner detector

The inner detector tracker of ATLAS covers  $|\eta| < 2.5$ . It is 7 m long and 1.2 m in radius. A 2 T magnetic field enables the momentum measurements. The tracker uses three different techniques to minimize the material and cost and to maximize the performance. Close to the interaction point are silicon pixels with a resolution of  $\sigma_{\phi r} = 12\mu\text{m}$ . There are 140 million readout channels in total. Outside the pixels are the silicon strips with a resolution of  $\sigma_{\phi r} = 16\mu\text{m}$ . The strips have 6 million channels and the astonishing area of 61 m<sup>2</sup> of silicon. The outer volume is covered with straw tubes providing drift time information combined with transition radiation to identify electrons. The resolution is  $\sigma_{\phi r} = 170\mu\text{m}$ .

The tracker performance can be approximated [13] (in units of TeV<sup>-1</sup> and mrad) by the parameterizations

$$\begin{aligned}\sigma\left(\frac{1}{p_T}\right) &= 0.36 \oplus \frac{13}{p_T \sqrt{\sin \theta}}, \\ \sigma(\phi) &= 0.075 \oplus \frac{1.8}{p_T \sqrt{\sin \theta}},\end{aligned}$$

where  $\oplus$  denotes the sum of squares.

## 4.2 Calorimetry

The calorimetry plays a central role in hadron colliders since it gives access to the rich physics of jets. The technique is robust, fast and has the nice property that the resolution in principle scales like  $1/\sqrt{E}$ . ATLAS has adopted the sampling calorimetry concept in different configurations, see Figure 3.

The electromagnetic (*EM*) calorimeter is LAr/Pb in an accordion structure to avoid cracks in azimuth and to enable efficient readout with small time constants. The requirements for the *EM* calorimeters are set extremely high. e.g. a dynamic range of 50 MeV to 3 TeV, linearity better than 0.5%, energy resolution better than  $1\% \oplus 10\%/\sqrt{E(\text{GeV})}$ , high granularity of the order  $\Delta\phi \times \Delta\eta = 0.03 \times 0.03$  and a good containment given by at least 24 radiation lengths of sampled material. The information is read out by 200,000 channels.

The hadronic calorimetry is LAr/Cu in the endcap region and in part of the forward. The forward region also has LAr/W for better resolution due to higher densities. The barrel and extended barrel regions consist of an Fe/Scintillator calorimeter with radial tiles staggered in depth. The main task for the hadronic calorimeter is

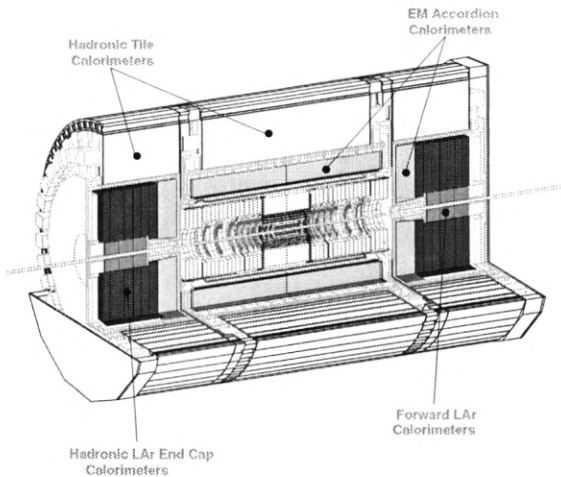


Figure 3: Overview of the different sampling calorimeters in ATLAS.

to improve the jet resolution, make sure that the energy is contained and to protect the muon system. Ten interaction lengths ( $\lambda$ ) of sampled material and  $1.5 \lambda$  of support fulfill this requirement. The resolution for jets should be better than  $3\% \oplus 50\%/\sqrt{E(GeV)}$  for  $|\eta| < 3$ , and  $10\% \oplus 50\%/\sqrt{E(GeV)}$  for  $|\eta| < 5$ .

### 4.3 The muon system

The large muon spectrometer covers the region  $|\eta| < 2.7$  with a trigger capability within  $|\eta| < 2.4$ . Superconducting air core toroid magnets provide the magnetic field. Monitored drift tubes provide most of the track measurements. The drift time is 700 ns and the wire resolution is 80  $\mu m$ . Where the rates are higher cathode strip chambers with a drift time of 30 ns are used. The system is monitored optically for a mechanical accuracy of 30  $\mu m$ . The trigger consists of resistive plate chambers in the barrel and thin gap chambers in the end-cap. The trigger chambers provide bunch crossing information and a second coordinate orthogonal to the precision measurement.

### 4.4 The trigger

In contrast to the low rate experiments at LEP, one would be blind in the LHC high rate environment without a sophisticated trigger. The bunches will collide at

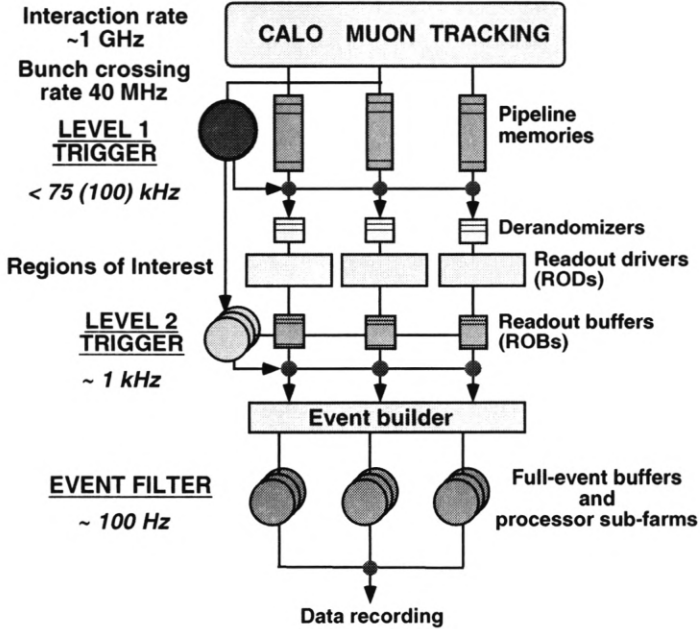


Figure 4: Overview of the trigger levels and the associated rates.

a rate of 40 MHz and generate on average 23 inelastic scatterings each time. The filtering of interesting events that are stored for final analysis is organized in three levels, see Figure 4. The first level identifies the bunch crossings and finds regions of interest (RoI) using  $p_T$  thresholds in the calorimeters and the muon system. The RoIs contain muons, *EM*-clusters, hadrons, and jets. Global information on missing transverse energy and scalar transverse energy is also reported. A decision of accept is taken within  $2\mu\text{s}$  and the information is passed on to level 2. Level 2 refines the RoIs selected by level 1 into physical objects that can be selected from a trigger menu. Depending on the luminosity option the thresholds are set as low as possible without saturating the readout chain and to allow different object mixtures during data taking. The final level 3 event filter (EF) decides whether or not the event should be stored. The EF uses offline software and the refinements are of such high quality that many of the rates are almost the same as the true signal.

## 5 Hadronic calorimetry

Electromagnetic cascades are governed by bremsstrahlung and pair production, hence they are characterized by the material constant called the radiation length ( $X_0$ ), where  $X_0$  is defined from the energy loss due to bremsstrahlung, i.e.  $dE/dx = -E/X_0$ . For iron  $X_0$  is 1.76 cm. The radial spread is dominated by multiple scattering and contained within approximately  $2R_M$ , where  $R_M$  is the Moliere radius. For iron  $R_M = 1.65$  cm. Hadronic cascades on the other hand are characterized by the nuclear interaction length ( $\lambda$ ) which for iron is 16.8 cm. The radial spread is caused by nuclear reactions with an average  $p_T$  of 350 MeV. Consequently both the longitudinal and radial spread are much larger for hadronic than for electromagnetic cascades. Also the fluctuations are larger due to the large variety of different possible processes.

The generic behavior and performance of sampling calorimeters for hadrons has been summarized in great detail by Wigmans [14, 15]. His main conclusion is that for an optimal performance, the response of the calorimeter to hadronic (h) and electromagnetic (e) components of the shower should be the same, i.e.  $e/h = 1$ . The calorimeter is then said to be compensating. That this is plausible is easily seen from the response in the calorimeter for a charged pion ( $\pi$ )

$$\pi = h(1-f) + ef$$

where  $f$  is the electromagnetic fraction which can be parameterized [16] by  $f \simeq 0.1 \ln E(\text{GeV})$ . After error propagation we have

$$(\sigma_\pi)^2 = (1-f)^2\sigma_h^2 + f^2\sigma_e^2 + (e-h)^2\sigma_f^2$$

and it is clear that the fluctuations in  $f$  will not affect the total resolution if  $e/h=1$ , assuming that the  $e/h$  tuning affects on  $\sigma_h$  and  $\sigma_e$  are small. For charged pions  $\sigma_f$  can be quite large due to the possible production of e.g. neutral pions in the initial interaction.

Any deviation from  $e/h = 1$  will result in a resolution scaling that deviates from the  $1/\sqrt{E}$  scaling which is expected from the sampling nature. According to Wigmans this deviation can be parameterized as a constant term

$$\frac{\sigma}{E} = \frac{a}{\sqrt{E}} + b.$$

The presence of a constant term will limit the intrinsic performance at high energies. However not only does the resolution deteriorate for  $e/h \neq 1$ , but the response will also no longer be linear in energy which is obvious from the ratio

$$\frac{e}{\pi} = \frac{e/h}{1-f(1-e/h)} \simeq A + B \ln E.$$

For small deviations from  $e/h = 1$  one can make a Taylor expansion giving the last expression where A and B are constants. It has been shown [17] that it is possible

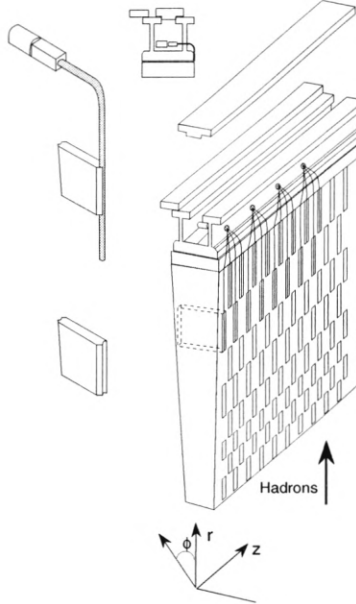


Figure 5: Schematic drawing of the Tile calorimeter.

under very specific conditions, to construct a compensating calorimeter using only passive elements like Pb/Scintillator. Since there exists no simulation tool that in a reliable way can predict the hadronic behavior much of the development is by trial and error. This is very much in contrast with electromagnetic simulation which is very predictive.

### 5.1 The Tile calorimeter

The Tile calorimeter [18, 19] covers the barrel ( $|\eta| < 1.0$ ) and extended barrel region ( $0.8 < |\eta| < 1.7$ ). The inner radius is 228 cm and the outer radius is 423 cm. The absorbing material consists of steel plates with 4 mm or 5 mm thickness. The sampling material is 3 mm thick polystyrene tiles doped with PTP and POPOP for optimal light yield and wavelength. The scintillator is wrapped in order to enhance the light yield and to provide a mask for uniform response. The light is collected and read out by wavelength shifting (WLS) fibers, one fiber on each side of the tiles. Due to the *EM*-calorimeter in front, only the hadronic response is optimized. This enables an unorthodox design with the tiles in the longitudinal direction. Good homogeneity is achieved by staggering in depth, and the fiber readout is made much simpler, see Figure 5.

The light from the WLS fibers is summed into an optimized segmented cell structure and detected by a photo multiplier tube (PMT), see Figure 6 for an example of

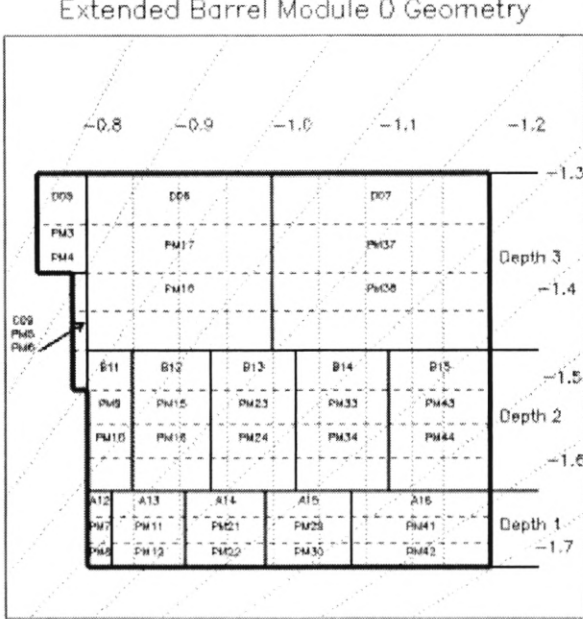


Figure 6: Mapping of cells and PMTs in the extended barrel module 0.

the cell to PMT mapping in the extended barrel. The cell structure for the barrel module 0 is shown in Figure 7. The output from the PMT is a 20 ns FWHM wide current pulse with a rise time of 5 ns. The total charge is proportional to the incoming light. The fast pulse puts strong requirements on the electronic readout. This is discussed in detail in the later sections. There are 64 azimuthal calorimeter modules containing 45 cells in the barrel and 14 cells in each of the two extended barrels. Each extended barrel also includes 3 PMTs for extra scintillators. There are in total about 10000 channels since there are two PMTs per cell.

One important parameter for the overall performance of the calorimeter is the light yield. The light yield is measured in number of photoelectrons  $N_{pe}$ , created in the PMT. According to Poisson statistics the statistical contribution to the resolution due to  $N_{pe}$  is expected to be of the order  $\sigma/E = 1/\sqrt{N_{pe}}$ . There are several ways to estimate  $N_{pe}$ . One can e.g. introduce known filters in the light path [20] or study the quantities  $\sigma_{LR} = L - R$  and  $E_{LR} = L + R$  [17], where L represents the left PMT and R the right PMT. In order not to severely affect the intrinsic resolution  $N_{pe}$  should be kept higher than 20 pe/GeV. This was achieved already in the 1993 test-beam of the first prototype with a  $N_{pe} = 24$  pe/GeV. Next year it was improved

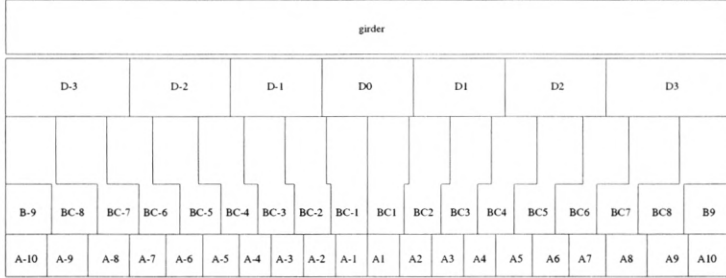


Figure 7: Cells in the barrel module 0.

to 48 pe/GeV, and finally the last prototype in 95 excelled with 64 pe/GeV. It is mainly the muons that are sensitive to  $N_{pe}$  and above 48 pe/GeV no measurable improvement was found except for an improved safety margin of course. In the 1997 test-beam of the extended module 0 the muon signal in the last compartment was separated from the noise by five standard deviations.

Since the  $e/h$  ratio is dependent on the sampling fraction the value will vary for different angles. In the prototypes  $e/h$  was measured to 1.23 at a 10 degree angle, and 1.36 at 20 degree angle. For the 1998 test-beam of the barrel module 0  $e/h$  was found to be 1.36 at  $\eta = -0.55$  and 1.45 at  $\eta = -0.25$ . The intrinsic resolution for the Tile calorimeter with respect to charged pions was measured in the 1996 barrel module 0 to be  $\sigma/E = 44\%/\sqrt{E(\text{GeV})} + 2.4\%$ . One might worry about the linearity but it has been shown in the 1996 test-beam with the combined  $EM$  and hadronic calorimeters that a weighting technique can reduce the nonlinearity to less than 2% with improved resolution. The weighting technique used was the so called H1 technique originally used at HERA [21]. The energy dependence of each cell is parameterized and the response for small energies is equalized upwards to the  $EM$  scale. The result for the combined setup using the H1 method was  $\sigma/E = (42\%/\sqrt{E} + 1.8\%) \oplus 1.8\%/E$ . The energy independent contribution to the spread is due to the high noise in the LAr accordion. The results for individual hadrons give confidence that the requirement on the jet resolution can be fulfilled since the individual hadron performance must be better than for jets.

## 5.2 Detector calibration and monitoring

No instrument is of any use unless it is stable and well calibrated. The Tile calorimeter is no exception. A lot of development has gone into providing fast and reliable methods to monitor the stability and recalibrate the complete detector chain, from an incoming particle to a digitized value in the analog to digital converter (ADC). These systems are described in the following subsections.

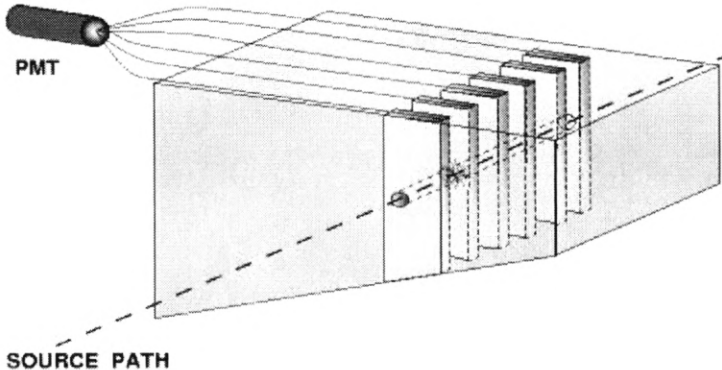


Figure 8: Conceptual picture of the Cs source as it moves through the detector during calibration.

### 5.2.1 Detector and PMT response via cesium 137

The  $^{137}\text{Cs}$  system is capable of monitoring the response from each tile and intercalibrate all PMT channels. It consists of a capsule of approximately 10 mCi  $^{137}\text{Cs}$  movable orthogonal through the iron and scintillating tiles, see Figure 8. The 30.2 y half life of the source is enough to provide monitoring over long periods of time. The 0.66 MeV  $\gamma$  radiation is also well tuned to resolve each tile. The PMT current is measured by an integrating ADC system, see Figure 9. By integrating the response cell to cell the PMT output can be equalized to give an overall intercalibration of the order of 2%. The PMT gain is controlled by adjusting the high voltage.

### 5.2.2 Laser surveillance of the PMT stability

Each PMT is connected to a pulsed laser via fibers. The pulse width is 15 ns. The laser output is monitored by three photodiodes which in turn are calibrated by a  $^{241}\text{Am}$   $\alpha$  source. Intensity modulation and filters enable linearity checks over the full dynamic coverage of the PMT readout chain. The laser can do drift checks in a matter of seconds and linearity scans in 10 to 15 minutes, e.g. between LHC fills.

### 5.2.3 Electronics calibration via charge injection

The fast readout that measures the PMT current must have an absolute calibration that is even better than the  $^{137}\text{Cs}$  system, that is below 1%. This is achieved by injecting charge( $Q$ ) stored in a known precision capacitor( $C$ ) at a well defined reference voltage( $U$ ), i.e.  $Q = CU$ . A conceptual diagram of the front-end input stage or "3-in-1 card" used in the final configuration that was tested 1998 is shown in Figure 10. The 3-in-1 card is integrated in the PMT block. It includes all the analog fast readout functionality except the ADC, see Figure 11. In the 1998 design  $U$  is set by a 10 bit DAC and two different  $C$  can be selected, either 100 pF

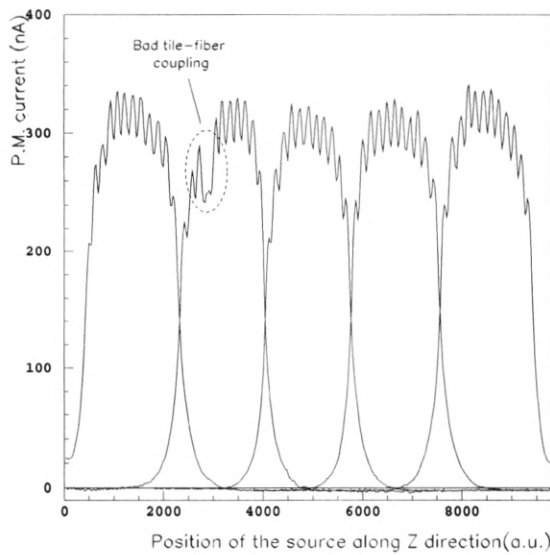


Figure 9: The response from the Cs system as the source is moved orthogonal through the iron and scintillating tiles.

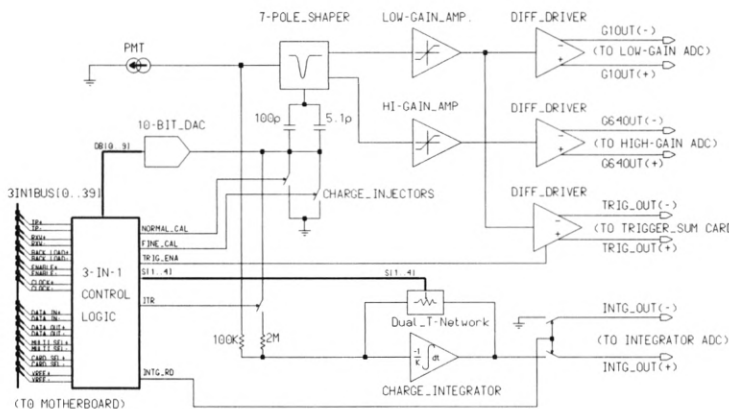


Figure 10: Conceptual diagram of the 1998 front-end analog electronics, physically realized in the 3-in-1 card.

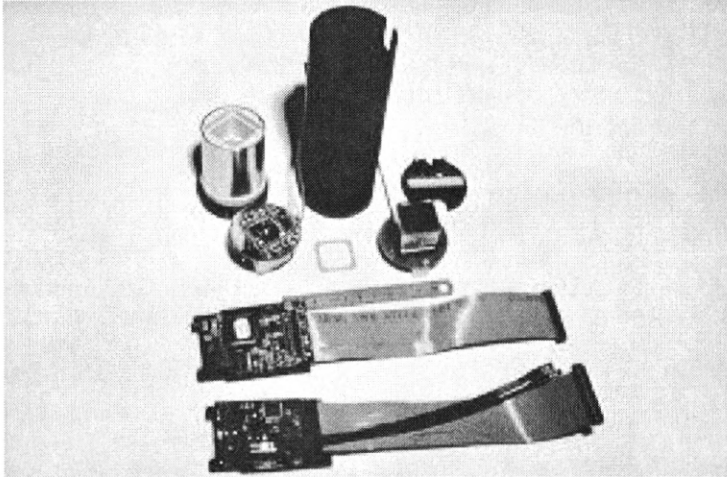


Figure 11: Picture of the PMT block with the integrated 3-in-1 card. The two black coaxial analog cables identifies the 3-in-1.

or 5.1 pF. Only the 100 pF is reliable for absolute calibration since it is less affected by parasitic capacitance,  $\sim 0.1$  pF. During 1998  $Q$  is given by

$$Q = 2 * 4.092 * C * DAC / 1023 \quad (\text{pC}) \quad (1)$$

The first version of the integrated charge injector used during 1996-1997 had only one capacitor but two 8 bit DACs. In 1996  $CU = 500$  pC, and in 1997  $CU = 640$  pC. The charge  $Q$  during 1996-1997 was

$$Q = CU * DAC1 * DAC2 / (255 * 255) \quad (\text{pC}) \quad (2)$$

Since the sampling interval is 25 ns and the FWHM of the pulse from the shaper is 50 ns there is no guarantee to sample the true peak during calibration. In order to resolve the pulse, a programmable delay is integrated in the 3-in-1 that enables a scan of the pulse by shifting the phase between the sample-and-hold and the charge injection. In most of the analysis the time step is set to  $\sim 0.4$  ns.

### 5.3 Fast readout electronics requirements

The lower bounds of constraints for the readout electronics performance are set by the physics requirements [24]. The low electronic noise needed to resolve minimum ionizing particles is incompatible on a fundamental level with the demand for accurate pulse timing and the rejection of the pile-up noise generated by the high bunch crossing rate, hence a delicate trade-off is necessary [22]. This trade-off is implemented in the shaper stage in the very beginning of the readout chain. It is

important to keep in mind that it is the output from the shaper that defines the requirements for the back-end of the system. The purpose of the shaper is to interface the fast photo-multiplier tube PMT pulse to the rest of the readout. The overall signal chain can be summarized as follows: the physics processes in the iron is sampled by scintillator tiles, the scintillator light is detected by the PMT generating 20 ns wide current pulses that are fed into the shaper input stage. This translates into a set of Tile specific readout requirements:

- Shaping 20 ns FWHM wide PMT signals into 50 ns FWHM wide and shape invariant pulses. The choice of 50 ns [23] was governed by the studies done for the LAr calorimeter. The more hostile environment in LAr required a pulse width between 47 ns and 80 ns. Due to low electronic noise figures and a completely passive and reactive shaper design the electronic noise is not an issue in Tile, e.g. the channel noise is 27 MeV and the muon deposition in the thinnest layer is 350 MeV. That 50 ns is quite safe from pile-up is clear from the pile-up factor of 1.18; that is, it is just 1.18 times more noisy than a measurement from one single bunch crossing, i.e. no pile-up present.
- A 30 MeV to 2 TeV (0.012 pC to 800 pC per channel) dynamic range equivalent to 16 bit on a linear scale. This is due to the physics requirement to resolve minimum ionizing particles (11 counts), while at the same time the system must not saturate when 2 TeV of energy is deposited in one cell.
- The readout must not affect the intrinsic calorimeter performance whose requirement is set in terms of the jet resolution:

$$\frac{\sigma}{E} = \frac{50\%}{\sqrt{E}} \oplus 3\%$$

- Dynamic distortions below 1%, in order to make use of robust digital filtering techniques.
- The channel to channel intercalibration spread must not exceed 1%.
- A sampling rate of 40 MHz given by the LHC[24] bunch crossing.
- For each event the complete readout chain must be able to deliver at least 5 signal samples and 2 pedestal samples at a rate of 75 kHz to the level 2 filter without dead time and withstand a radiation dose of 10 to 50 krad. These requirements are not covered in this paper, however the tests for the final digitizer system began already during the end of the 1998 test-beam[25].

## 6 Jets in the ATLAS detector

The concept of collimated hadrons with high multiplicity as the result of a fragmentation process appeared already in the end of the 60's in deep inelastic scattering, see e.g. [26]. The first really convincing experimental evidence for hadronic jets came from dijet events observed in 1975 in  $e^+e^-$  collisions [27]. However, before we can say anything qualitative, the notion of a jet has to be defined. The first and most popular, at least for hadron collisions, is due to Sterman and Weinberg [29]. They demonstrated in 1977 a divergence free observable in terms of cross-section for the energy flow within a cone, using leading order QCD calculations. This class of jet algorithms, not unexpectedly, goes under the name of cone algorithms. As a consequence of the calculation they also concluded that dijet events will dominate at high energies as a result of the asymptotic behavior of the coupling constant in QCD. The default cone definition is due to the Snowmass accord [28], where the boost invariant jet observables are

$$E_T = \sum_i E_{T_i},$$

$$\eta = \sum_i \frac{E_{T_i} \eta_i}{E_T},$$

$$\phi = \sum_i \frac{E_{T_i} \phi_i}{E_T}.$$

The index  $i$  represents all particles within the cone  $R$ , where  $R$  is defined as  $R = \sqrt{\delta\eta^2 + \delta\phi^2}$ .  $R$  is typically between 0.4 and 0.7. The energy  $E_T$  is the transverse energy relative to the beam axis, i.e.  $E_T = E \sin \theta$ . The cone algorithm defines the jet in terms of two thresholds:  $E_{seed}$  and  $E_{jet}$ . The algorithm is

1. For each cell in the  $(\eta, \phi)$  plane initiate a jet if the cell energy is larger than  $E_{seed}$ . The jet direction is given by the jet seed.
2. Sum all cells within the cone  $R$  around the jet direction. If the new jet axis does not coincide with the jet seed, iterate until a stable direction is achieved.
3. Keep the jet if the energy is larger than  $E_{jet}$ . Repeat 1 until there are no cells left.

In the analysis that follows, the iterative procedure is not included, and any jet overlap is not treated.

Later it has become more and more evident that the definition should be what is called infrared and collinear safe in order to easily compare measured quantities to higher order calculations. This property is not intrinsic for the cone algorithm, however the situation can be greatly improved by modifications of the iterative version [34]. An approach that is intrinsically safe is the so called  $k_T$  algorithm [32, 33] inspired by the clustering technique [30]. The main reason for the popularity of the

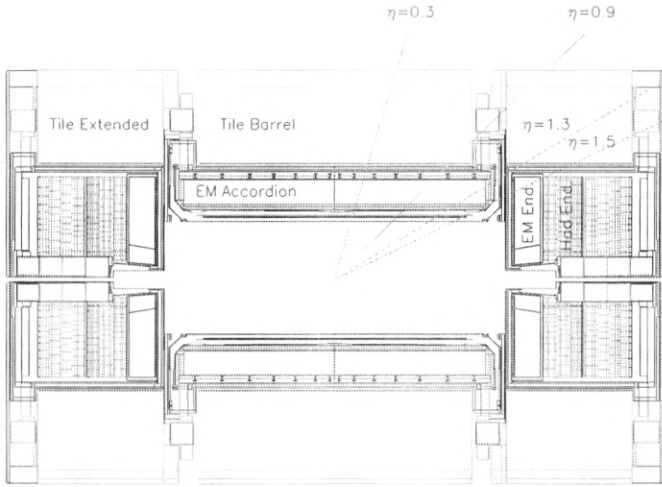


Figure 12: Overview of the ATLAS calorimetry volumes, as defined in the GEANT detector simulation.

fixed cone, especially in hadron colliders, is that it is easier to control instrumental effects than for the clustering technique.

From the physics point of view there are many reasons for being interested in jets. Apart from QCD, Higgs and the top quark are the good examples. If for example Higgs is a SUSY Higgs, it is very likely that the first evidence will appear as an excess in the  $b\bar{b}$  invariant mass spectrum. Measurements of the top quark which also are very important both for the SM and for finding new physics, constitute the state of the art in jet spectroscopy. And for searches of SUSY, jets are extremely important since the dominating production mechanism of SUSY particles is through squarks and gluinos.

## 6.1 Jet reconstruction

To cover all aspects of jet reconstruction is very difficult since even without the instrumental effects included, there are many non trivial issues: out-of-cone QCD radiation, soft underlying events, differences in the fragmentation etc. What I will try to do is to highlight the experimental aspects of jet reconstruction in the ATLAS barrel calorimeter and indicate the energy resolution performance using very basic techniques. A more detailed description can be found in Paper I.

As we can see in Figure 12, the jets are measured by a large set of calorimeters

that have very different behaviors<sup>3</sup>. The picture is further complicated by the existence of unsampled or "dead" material inhomogeneously distributed in the detector. The dead material is found e.g. in the beam pipe, inner detector, cryostat walls, support structures and the coil.

The dominating experimental contributions to the jet energy resolution are the non compensation, losses in dead material, out-of-cone showers and noise. The investigation of all these effects requires full detector simulation. In this case a very detailed description of the ATLAS detector is implemented in GEANT [31]. The jets are light quark dijets events generated at fixed  $\eta$  and energy. For the energy losses found in dead material volumes see Figure 13. The jet energy response using only the electromagnetic scale calibration is shown in Figure 14. In Figure 14 we see that the jet energy reconstructed at the electromagnetic scale depends both on the energy scale due to the non compensation, and on the cone size since the jets become narrower at higher energies. The non compensation is reduced by energy dependent weighting which makes use of the calorimeter segmentation. The energy deposited in dead material can be estimated by the geometrical mean of the energy detected in compartments surrounding the dead volumes and by the use of extra scintillators sampling the shower. The noise level will influence the weighting in such a way that compartments with low signal to noise will be given smaller weights. In order to disentangle the instrumental effects on the jet energy reconstruction, the jet energy response within a cone in the calorimeter is compared to a "true" cone energy  $E_{true}$  constructed by the fragmented particles. The only experimental effect applied to the true particles is the bending in the magnetic field. The weighting and the calibration are performed by optimizing the expression

$$\min_{w_i} \sum_j \left( \sum_i w_i E_{ij} - E_{truej} \right)^2,$$

where compartments are sections of the calorimeter which behave in a similar way, or estimators of dead energy. For further details see Paper I.

---

<sup>3</sup>The possibility to improve the resolution by using charged tracks in the inner detector is not studied. However the dead material in the inner tracker is included in the simulations.

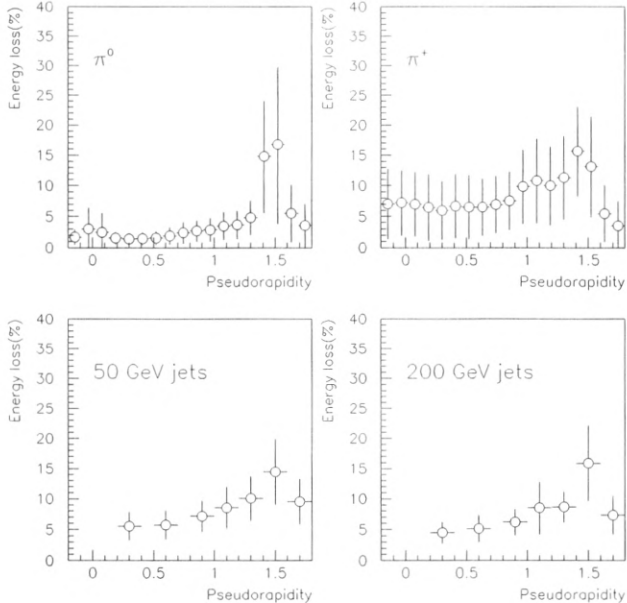


Figure 13: Energy lost in dead material. Jets are mostly a mixture of pions. The energy lost by  $\pi^0$  is shown in the upper left figure and the one by  $\pi^+$  in the upper right one. The vertical error bars represent the actual RMS of the distribution, not the error of the mean. One sees that the dead material is concentrated in a small window of about 0.2 in  $\eta$  at  $|\eta|=1.45$ . For charged pions, there are two components, the dead material in front of the calorimeter and the dead material between the EM and HAD calorimeters due to the outer cryostat wall. In the barrel there are larger fluctuations on the hadronic energy loss due to the fluctuation of the starting point of the hadronic shower.

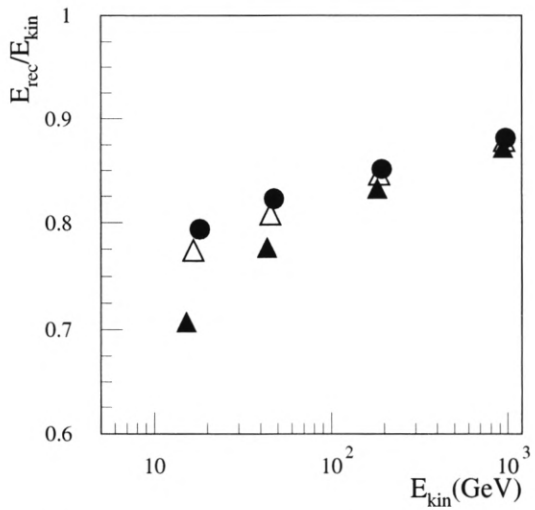


Figure 14: Mean relative reconstructed jet response using the *EM* calibration only at  $|\eta| = 0.3$ .  $R=0.4$  (filled triangles),  $R=0.7$  (open triangles) and  $R=1.5$  (filled circles). For  $R=1.5$  the response is close to the full calorimeter response, hence the non compensation and energy lost in dead material are the main contributions. For smaller cones like  $R=0.4$ , out-of-cone showers become important at low energies. The energy variable  $E_{\text{kin}} = E_{\text{true}}$ .

## 6.2 Results

The main result from the simulations is the jet energy resolution. This is to be compared to the requirements for jets which is

$$\frac{\sigma}{E} = \frac{50\%}{\sqrt{E}} \oplus 3\%.$$

Scans are made both in energy and in  $\eta$ . The resolution for fixed energies are shown in Figure 15. An energy parameterization of the resolution is shown in table 1 according to the expression

$$\frac{\sigma}{E} = \frac{a}{\sqrt{E}} \oplus b \oplus \frac{c}{E},$$

where  $c$  is the energy independent contribution to the energy resolution  $\sigma$ , e.g. electronic noise. This study confirms previous results [35] and no alarming degradation is found due to the inclusion of more dead material in the updated geometry. Even with a very simple weighting procedure the performance conforms to the requirements. One should however be aware of the reduced energy resolution when using small cones in the crack region due the large fluctuations of energy lost in dead material.

Cone	$\eta$	$a(\%GeV^{1/2})$	$b(\%)$	$c_{0\sigma}(GeV)$	$c_{2.5\sigma}(GeV)$
0.7	0.3	$52.3 \pm 1.1$	$1.7 \pm 0.1$	$3.0 \pm 0.1$	$2.0 \pm 0.1$
0.4	0.3	$62.4 \pm 1.4$	$1.7 \pm 0.2$	$2.0 \pm 0.1$ ( $4.7 \pm 0.2$ )	$1.7 \pm 0.2$
1.5	0.3	$48.2 \pm 0.9$	$1.8 \pm 0.1$		
0.7	0.9	$63.0 \pm 1.5$	$2.0 \pm 0.3$	$2.7 \pm 0.2$	
0.4	0.9	$74.7 \pm 2.1$	$2.7 \pm 0.5$	$1.9 \pm 0.3$	
0.7	1.3	$66.1 \pm 2.1$	$3.4 \pm 0.2$	$2.9 \pm 0.2$	
0.4	1.3	$82.3 \pm 2.6$	$4.0 \pm 0.3$	$2.0 \pm 0.3$	

Table 1: Parameterization of the jet resolution. During the fit of the noise term, the  $a$  and  $b$  parameters are kept fixed. The  $c$  term is given for two different cell cuts, either at  $0\sigma$  or  $2.5\sigma$  of the noise. The parenthesis includes pile-up effects.

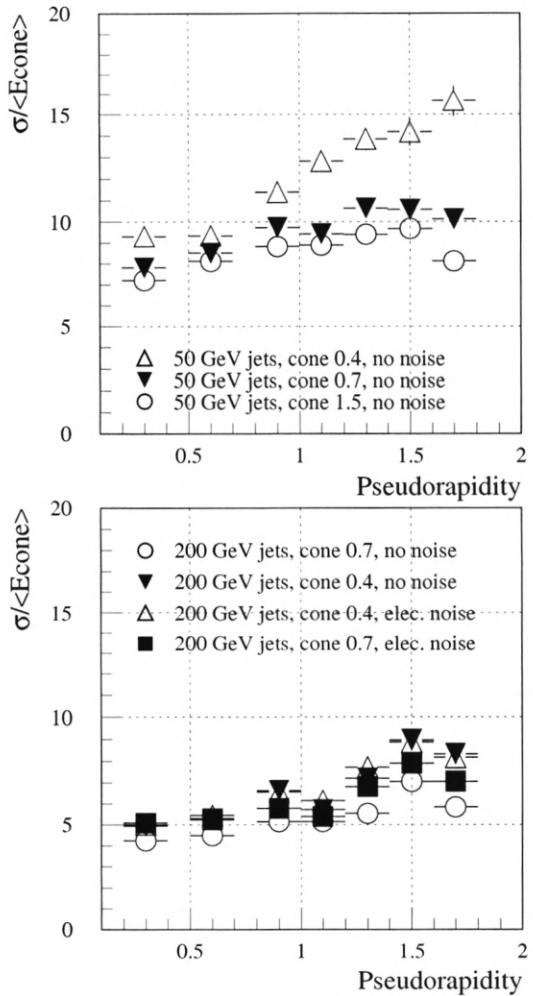


Figure 15: Energy resolution for 50 GeV and 200 GeV jets.

## 7 Signatures of supersymmetry

There are two classes of symmetries: internal and external symmetries. External symmetries are the symmetries of space-time itself. To our current knowledge it is enough to require that space-time transforms according to the symmetries given by the Poincaré group, that is the Lorentz group plus translations. The invariants (or Casimirs) of the Poincaré group are, for a massive object, only dependent on the rest mass and the spin [36]. Thus, the conclusion is that spin is a quantity associated with external symmetry. In the continuous search for new physics (symmetries) in nature one can ask: how can the external symmetries of space-time be extended? According to a theorem by Haag, Lopuszanski and Sohnius [37] there is only one way to extend the Poincaré symmetry of the S-matrix, this extension is called supersymmetry (SUSY). The supersymmetry extension consists of commutator and anti-commutator relations between the generators of the Lorentz group and the supersymmetry generators  $Q$

$$\begin{aligned} [P^\mu, Q_\alpha] &= 0, \\ [M^{\mu\nu}, Q_\alpha] &= -\frac{1}{2}(\sigma^{\mu\nu})^\beta_\alpha Q_\beta, \\ [M^{\mu\nu}, \bar{Q}_{\dot{\alpha}}] &= -\frac{1}{2}Q_{\dot{\beta}}(\bar{\sigma}^{\mu\nu})^{\dot{\beta}}_{\dot{\alpha}}, \\ \{Q_\alpha, Q_\beta\} &= \{\bar{Q}_{\dot{\alpha}}, \bar{Q}_{\dot{\beta}}\} = 0, \\ \{Q_\alpha, \bar{Q}_{\dot{\alpha}}\} &= 2\sigma^\mu_{\alpha\dot{\beta}}P_\mu. \end{aligned}$$

where  $P^\mu$  is the energy-momentum tensor and  $M^{\mu\nu}$  is the angular momentum tensor. Since there are anti-commutators this is referred to as graded Lie algebra. The undotted  $Q$  transforms as a 2-component left-handed spinor and the dotted as a right-handed spinor.  $Q$  changes the spin by one-half, thus there must exist a corresponding boson to each fermion and vice versa. We see that  $[P^\mu P_\mu, Q_\alpha] = 0$ , which means that the mass is the same for a particle and its supersymmetric partner. It is obvious that supersymmetry must be broken at low energies since no supersymmetric particle has yet been found.

If we want to make a minimal extension of the SM that is supersymmetric we get a model that is referred to as MSSM [38]. In MSSM every particle has a supersymmetric partner (sparticle), distinguished from the SM particles in text by a tilde, e.g.  $\tilde{B}$ . The supersymmetric part of MSSM contains no additional parameters except  $\tan\beta$ , which is the ratio between the VEV of the two Higgs fields. MSSM must have two Higgs doublets in order to be free of anomalies. Out of these two doublets five fields are physical: one is  $CP$ -odd and neutral, two are  $CP$ -even and neutral and two are charged. The same simplicity concerning the number of new parameters is not true for the part responsible for the breaking of supersymmetry. There are 123 parameters in the so called soft terms in the non supersymmetric Lagrangian. They consist of mass terms, bi-linear and tri-linear scalar couplings. The general MSSM Lagrangian contains unacceptable terms that violates baryon and lepton conservation. To make the model phenomenologically

acceptable one normally imposes a symmetry called *R*-parity. The consequence of *R*-parity is that the lightest SUSY particle (LSP) is stable (and neutral due to cosmological reasons), and the SUSY particles must be produced in pairs. There is however no direct theoretical reason to expect *R*-parity to be conserved. It is possible to construct stable proton SUSY models with *R*-parity violating terms in the Lagrangian. Therefore it is highly relevant to put limits on the *R*-parity violating couplings. If *R*-parity is violated the LSP will decay and the experimental SUSY signatures will change drastically.

Aside from the aesthetic beauty of supersymmetry, there are also direct motivations for the possibility of supersymmetry at higher energies. If we insist that the SM is an effective theory, that is we impose an energy scale  $\Lambda$  for new physics with new degrees of freedom, we find that the renormalization of the scalar mass at very high energies needs tremendous fine tuning due to a quadratic dependence on  $\Lambda$ . This is not natural. If there were no such scale there would be no problem since the SM is renormalizable, period. However, there is at least one very natural new physics scale where something new is likely to happen since at that scale the metric is expected to receive wild quantum fluctuations. That scale is the Planck scale

$$M_P = G_N^{-1/2} \simeq 10^{19} \text{ GeV},$$

where  $G_N$  is Newtons constant. At  $M_P$  the gravitational force is comparable in strength to the other forces. If we have exact supersymmetry, the fermionic and the bosonic quantum loop contributions cancel and the renormalized theory remains the same at any scale. The supersymmetry is broken by the soft terms in the MSSM Lagrangian, but the soft breaking terms introduce only a logarithmic dependence on  $\Lambda$  which make the quantum corrections stable.

Another strong argument for SUSY is that if the measured gauge couplings are evolved to high energies using the SM RGE they fail to unify at any scale. Gauge coupling unification is a common prediction of Grand Unified Theories [39]. The MSSM RGE on the other hand tend to unify at the intriguing scale  $M_{GUT} \simeq 0.001 M_P$ .

## 7.1 Supersymmetry breaking

The most important topic in SUSY is actually the origin of supersymmetry breaking (SSB), both theoretically and experimentally. To spontaneously trigger SSB within MSSM itself turns out to be very difficult due to the super trace theorem that forbids SSB at tree level. A successful approach is instead to assume that the SSB origin is communicated radiatively from a hidden sector into MSSM by flavor blind interactions. Gravity is just such a flavor blind interaction that appears naturally once SUSY is required to be a local symmetry [40]. The scenario with gravity mediated SSB is called SUGRA. Assuming that SSB takes place at  $\sqrt{F} \sim 10^{11}$  GeV one finds by dimensional analysis the mass scale for soft SUSY breaking ( $m_{soft}$ ) to be of the order

$$m_{soft} \sim \frac{F}{M_P} \sim 100 \text{ GeV}.$$

SUGRA is a very beautiful effective theory where all the non renormalizable soft terms can be described with only five parameters:  $m_{1/2}$ ,  $m_0^2$ ,  $A_0$ ,  $\tan \beta$  and  $\text{sgn}(\mu)$ . The first three are the common fermionic mass, the common scalar mass and a trilinear coupling. The last two stem from the requirement of electro-weak symmetry breaking. Consequently the complete particle spectrum is predicted and the lightest neutral supersymmetric particle (LSP) turns out to be a neutralino ( $\chi_1^0$ ), a mixture of  $\tilde{B}$ ,  $\tilde{W}^3$ ,  $\tilde{H}_u^0$ , and  $\tilde{H}_d^0$ .

In minimal SUGRA universal masses and couplings are imposed at the GUT scale to assure GUT and small FCNC. These assumptions are very strong. Another way to suppress FCNC is to assume that pure gauge interactions communicate the SSB. A layer with messengers at the mass scale  $M_m$  is put in between MSSM and the true and somewhat unspecified source of SSB. Now the boundary conditions are closer in energy to the SM and the gauge fields automatically suppress FCNC. This scenario is referred to as gauge mediated SSB (GMSB)[41]. Now we have e.g.  $M_m \sim \sqrt{F_m} \sim 10^5$  GeV

$$m_{\text{soft}} \sim \frac{\alpha_i}{4\pi} \frac{F_m}{M_m} \sim 100 \text{ GeV},$$

where the  $\alpha_i$ 's are the usual gauge couplings. Realistic GMSB is quite complicated and a practical model was first proposed by Dine et al[42] inspired by a suggestion from Ed Witten. The messengers are chiral superfields in a representation of  $SU(5)$  in the minimal case. Different field configurations can be parameterized by a parameter called  $N_5$ . Depending on  $M_m$  the maximum of  $N_5$  ranges from 5 to 10 in order to preserve perturbativity[43]. GMSB can be made very predictive and the minimal model is fixed by only six parameters:  $M_m$ ,  $F_m$ ,  $F$ ,  $N_5$ ,  $\tan \beta$  and  $\text{sgn}\mu$ .  $F$  is the fundamental SSB scale while  $F_m$  is what the messengers see.  $F$  determines the gravitino ( $\tilde{G}$ ) mass

$$m_{3/2} \sim \frac{F}{M_P} < 1 \text{ keV}$$

and hence  $\tilde{G}$  is the LSP in GMSB models. The phenomenology is mainly determined by the next-to-lightest sparticle (NLSP).

## 7.2 $\tilde{\tau}$ as the NLSP in ATLAS

At the LHC the typical production cross-section via strong interaction for SUSY events is expected to be of the order  $\mathcal{O}(1)$  pb or more for masses that are phenomenologically relevant (2 TeV or less) [44]. Since the initial luminosity is  $10 \text{ fb}^{-1}/\text{yr}$ , the matter of discovery will not be problematic. This is particularly true if R-parity is conserved. More critical will be to determine the model and the model parameters once SUSY is discovered. In order to make any realistic estimations of the sensitivity one has to select a particular model since the decay chain and the final states can be very different from model to model. Useful handles in the understanding of the underlying mechanism for SSB are the event topology and the sparticle masses. It has been shown in explicit models that many sparticle masses

Point	$\Lambda_m$ [TeV]	$M_m$ [GeV]	$N_5$	$\tan \beta$	$\text{sgn } \mu$	$C_{grav}$
G3a	30	250	3	12	+	1
G3b	30	250	3	12	+	5000

Table 2: The GMSB model parameters.

[13, 45] can be measured model independently with the only requirement that R-parity is conserved and that there exists a decay chain. These techniques are based on forming invariant masses from final states at the end of the decay chain and measuring the edges. ATLAS has investigated both SUGRA and GMSB models and shown that in these cases the model parameters can be determined to very high precision. In case of GMSB most of the parameter space has been covered in reference [46]. However, one very important domain of the parameter space that has  $\tilde{\tau}$  as the NLSP was not considered. This is one of the subjects of this thesis.

### 7.2.1 The model

The GMSB model is specified by the six parameters in Table 2.  $\Lambda_m = F_m/M_m$  is the effective SUSY breaking scale, and  $C_{grav} \sim F/F_m$  is the gravitino scaling factor which controls the lifetime of the NLSP. The NLSP lifetime has been studied both for a short lifetime with a decay at the interaction vertex ( $C_{grav} = 1$ ), and for a quasi-stable case when the NLSP decays outside of the detector ( $C_{grav} = 5000$ ). For more details concerning the model the reader is referred to the manual of the Monte Carlo generator ISAJET [47] which was used for the event generation.

### 7.2.2 Analysis

The mass spectra given by ISAJET for the model G3 compared to another model G2 analyzed in reference [46] with a lower  $\tan \beta = 5$  is shown in Table 3. We see that the NLSP is the lightest  $\tilde{\tau}$  which is called  $\tilde{\tau}_1$ . Due to mixing effects and the strong coupling to the Higgs sector, a common feature of MSSM is that  $\tilde{\tau}$  tend to be light when  $\tan \beta$  is large. This is explicitly clear from the mass spectrum as  $\tan \beta$  is increased from 5 to 12. The consequence is that  $\tilde{\tau}$  no longer is degenerate with the other sleptons, which is the case in model G2a and G2b studied in reference [46] where sleptons are co-NLSP. The experimental difference is that G3 has taus in the final states which are much more difficult to measure than muons and electrons. A typical example of a decay chain for a squark from the sparticle pair production is

$$\tilde{q}_R \rightarrow \tilde{\chi}_{1,2}^0 q \rightarrow \tilde{l}_R^- l^+ q \rightarrow \tilde{\tau}_1(\tau) l^- l^+ q \rightarrow \tilde{G} \tau(\tau) l^- l^+ q.$$

The tau in parenthesis has low transverse momentum due to the limited available phase-space and will most probably escape detection. If the NLSP is quasi-stable it will show up as a spectacular heavy charged particle in the muon-spectrometer [48]. This is a very clear signal with low backgrounds, and enables enough measurements

Particle	G2	G3	Particle	G2	G3
$\tilde{g}$	699	699			
$\tilde{u}_L$	658	658	$\tilde{u}_R$	635	635
$\tilde{d}_L$	662	662	$\tilde{d}_R$	634	634
$\tilde{t}_2$	674	672	$\tilde{t}_1$	577	582
$\tilde{b}_2$	640	644	$\tilde{b}_1$	631	626
$\tilde{e}_L$	204.1	204.5	$\tilde{e}_R$	102.7	103.3
$\tilde{\tau}_2$	204	207	$\tilde{\tau}_1$	101.6	97.4
$\tilde{\nu}$	189	188	$\tilde{\nu}_\tau$	189	188
$h^0$	106	111	$H^0$	337	311
$A^0$	334	311	$H^\pm$	344	321
$\tilde{\chi}_1^0$	113.9	115.5	$\tilde{\chi}_2^0$	196.2	196.1
$\tilde{\chi}_3^0$	277	265	$\tilde{\chi}_4^0$	329.9	316.5
$\tilde{\chi}_1^\pm$	191.8	193.0	$\tilde{\chi}_2^\pm$	328	316

Table 3: Masses in GeV as  $\tan \beta$  is increased from 5 (G2) to 12 (G3). Note that  $\tilde{e}$  and  $\tilde{\mu}$  are degenerate. The model G2 was investigated in [46]. The sleptons are co-NLSP in this case.

to fix the model parameters. However, for the short lifetime NLSP the experimental situation is much more challenging. Fortunately the same flavor opposite signed leptons provide lots of information and a good separation from the background. A detailed analysis (see paper II) reveals, somewhat surprisingly, that even the short lifetime scenario provides a sufficient number of mass measurements such that the model can be determined to high precision. The reason is mostly due to the power of forming invariant masses. An example taken from the end of the decay chain is the invariant mass of the tau and the softest lepton which has an upper edge at

$$\begin{aligned} M_{\tau l}^{max} &= \sqrt{M_{\tilde{l}_R}^2 - (M_{\tilde{\tau}_1} + M_\tau)^2} = \\ &= 29.0 \text{ GeV } (29.2 \pm 1 \text{ GeV}), \end{aligned}$$

where the numbers within parenthesis are from the fit. The mass spectra is shown in Figure 16 with a clear measurable edge and a low level of SM background.

### 7.2.3 Results

The result is a sufficient number of measured sparticle masses such that the GMSB model can be determined. The mapping from the sparticle masses back to the originating model is implicitly given by the GMSB mass relations [43] which at leading order are proportional to  $N_5 \Lambda_m$  for the gaugino masses, and  $\sqrt{N_5} \Lambda_m$  for the slepton masses. There is also an overall logarithmic dependence on  $M_m$  from to the boundary conditions for the renormalization group equations. Notice however, that  $C_{grav}$  is an independent parameter provided by a NLSP lifetime measurement which

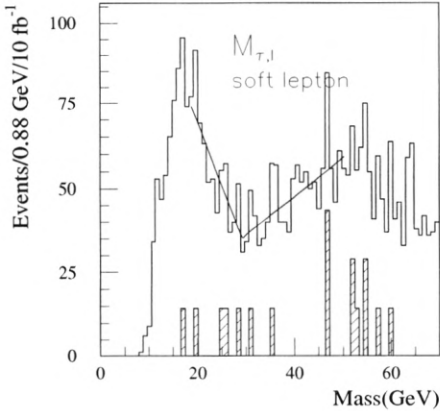


Figure 16: The invariant mass spectra for a hard tau and a soft lepton. The hatched area is the SM background.

is not covered in this analysis. The analysis provides six mass measurements for the G3a model

$$\begin{aligned}
 M_{ll}^{max} &= M_{\tilde{\chi}_1^0} \sqrt{1 - \frac{M_{\tilde{l}_R}^2}{M_{\tilde{\chi}_1^0}^2}} \sqrt{1 - \frac{(M_{\tilde{\tau}_1} + M_\tau)^2}{M_{\tilde{l}_R}^2}} = 14.5 \text{ GeV } (14.3 \pm 0.1 \text{ GeV}), \\
 M_{ll}^{max} &= M_{\tilde{\chi}_2^0} \sqrt{1 - \frac{M_{\tilde{l}_R}^2}{M_{\tilde{\chi}_2^0}^2}} \sqrt{1 - \frac{(M_{\tilde{\tau}_1} + M_\tau)^2}{M_{\tilde{l}_R}^2}} = 46.8 \text{ GeV } (42.3 \pm 5 \text{ GeV}), \\
 M_{l\bar{l}_j}^{max} &= M_{\tilde{q}_R} \sqrt{1 - \frac{M_{\tilde{\chi}_1^0}^2}{M_{\tilde{q}_R}^2}} \sqrt{1 - \frac{(M_{\tilde{\tau}_1} + M_\tau)^2}{M_{\tilde{\chi}_1^0}^2}} = 320 \text{ GeV } (313 \pm 6 \text{ GeV}), \\
 M_{l\bar{l}_j}^{max} &= M_{\tilde{q}_L} \sqrt{1 - \frac{M_{\tilde{\chi}_2^0}^2}{M_{\tilde{q}_L}^2}} \sqrt{1 - \frac{(M_{\tilde{\tau}_1} + M_\tau)^2}{M_{\tilde{\chi}_2^0}^2}} = 546 \text{ GeV } (530 \pm 5 \text{ GeV}), \\
 M_{\tau l}^{max} &= \sqrt{M_{\tilde{l}_R}^2 - (M_{\tilde{\tau}_1} + M_\tau)^2} = 29.0 \text{ GeV } (29.2 \pm 1 \text{ GeV}), \\
 M_{\tau l}^{max} &= \sqrt{M_{\tilde{\chi}_1^0}^2 - M_{\tilde{l}_R}^2} = 51.7 \text{ GeV } (51.1 \pm 1 \text{ GeV}).
 \end{aligned}$$

These six equations can be used to solve for the six unknown sparticle masses. Together with the independent measurements of the NSLP lifetime and the lightest Higgs mass they provide enough constraints to fix the underlying GMSB model.

## 8 $CP$ violation beyond the Standard Model

$CP$  violation has played an important part in the development of the SM. The reason is that any symmetry violation gives vital clues to the structure of the underlying model. The  $CP$  violation observed in experiments performed on the neutral kaon and the B-meson systems is compatible with the SM. This however, does not mean that there cannot be any other sources of  $CP$  violation. It may very well be that the level of non SM  $CP$  violation is weak in these processes. A particularly interesting sector to search for new physics is the top sector. The top quark is about forty times heavier<sup>4</sup> than any other matter particle due to its large Yukawa coupling to the Higgs VEV. This makes it interesting for at least two reasons: it is closer to the border of unexplored energy domains, and it is sensitive to  $CP$  violation in the Higgs sector. Nature has been kind to us such that the level of CKM induced  $CP$  violation in the top sector is extremely small. As an example we can look at the partial rate asymmetry which is a common observable for  $CP$  violation in the SM

$$\mathcal{A} = \frac{N(t \rightarrow W^+ b) - N(\bar{t} \rightarrow W^- \bar{b})}{N(t \rightarrow W^+ b) + N(\bar{t} \rightarrow W^- \bar{b})} = \frac{\Gamma(t \rightarrow W^+ b) - \Gamma(\bar{t} \rightarrow W^- \bar{b})}{\Gamma(t \rightarrow W^+ b) + \Gamma(\bar{t} \rightarrow W^- \bar{b})}.$$

This quantity has been calculated in reference [51] and serves well to illustrate why the  $CP$  violation is so small. Already the fact that the CKM element  $V_{tb} \simeq 1$  gives a hint since there must be a competing decay channel to enable  $CP$  violation of the partial rate, and in this case there is not much room left. Any  $CP$  violation has its origin in a complex phase that cannot be rotated away. For the partial rate the  $CP$  violating phase emerges due to the interference between the tree and the one loop amplitudes, see Figure 17. For the top channel we have (see section 2.5)

$$d\Gamma(t \rightarrow W^+ b) = (A_1 + A_2)(A_1^* + A_2^*) \frac{d\Phi_f}{2m_t} = (|A_1|^2 + |A_2|^2 + 2\Re(A_1 A_2^*)) \frac{d\Phi_f}{2m_t},$$

where  $A_1$  is the tree level amplitude,  $A_2$  is the one loop amplitude and  $\Phi_f$  is the phase-space element. The asymmetry is given by

$$\mathcal{A} = \frac{\int d\Phi_f (\Re(A_1 A_2^*) - \Re(\bar{A}_1 \bar{A}_2^*))}{\int d\Phi_f (\Re(A_1 A_2^*) + \Re(\bar{A}_1 \bar{A}_2^*))} < \mathcal{O}(10^{-9}),$$

which is far beyond the experimental reach. This is precisely what we want in order to be sensitive to new physics.

### 8.1 Effective theory of $CP$ violation in $t\bar{t}$ production

At the moment there is no evidence that there exist beyond SM  $CP$  violating sources, except perhaps that the level of SM  $CP$  violation may not be enough for Sakharov's conditions for baryogenesis [52]. But, at the same time there is almost an infinite

---

<sup>4</sup>Maybe it is more correct to say that all other particles have unnaturally small masses since the VEV is 246 GeV and the top mass is 175 GeV. The small coupling is a form of fine tuning.

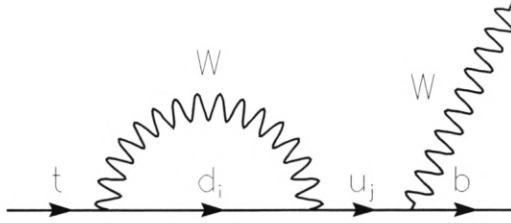


Figure 17: The one loop self-energy diagram  $A_2$  that contributes to the SM  $CP$  violation in the asymmetry observable  $\mathcal{A}$ .

set of potential models that are not ruled out. Therefore it makes sense to neglect the details of the mechanism that might induce the  $CP$  violation, and focus on the experimental question if there exists  $CP$  violation in a particular process up to a certain energy scale. We would like to have a limited set of handles on the  $CP$  violation, most preferable one single parameter. One way to achieve this is to ask the following question: what are the leading order terms allowed in the Lagrangian that concerns the production of top quark pairs if we are only interested in making predictions below a fixed energy scale  $\Lambda$ ? Please notice that we here only look at the production<sup>5</sup>. It turns out that the symmetries of Lorentz invariance and the SM put severe limits on the structure of the allowed operators that can be used. For  $CP$  violating terms we know that there is only the CKM mechanism within the SM<sup>6</sup> so we have to relax the requirement of renormalizability and allow terms of mass dimensions higher than four. All leading order, i.e. mass dimension six,  $CP$ -odd and  $CP$ -even operators regarding the third family have been classified in reference [54, 55]. Out of these there are only three operators that are relevant for top pair production. They are

$$\begin{aligned}\mathcal{O}'_{qG} &= i\bar{q}_L \gamma^\mu D^\nu q_L G_{\mu\nu}, \\ \mathcal{O}'_{tG} &= i\bar{t}_R \gamma^\mu D^\nu t_R G_{\mu\nu}, \\ \mathcal{O}_{tG} &= \bar{q}_L \sigma^{\mu\nu} t_R \tilde{\Phi} G_{\mu\nu}.\end{aligned}$$

Fortunately they are all related up to four-point fermion vertices by the use of the SM equations of motion [63]. Hence, from one of these operators we can construct

---

<sup>5</sup>It is equally possible that the  $CP$  violation is present in the decay. However, the effects are likely to be very small, see for example reference [53].

<sup>6</sup>There is also the possibility of the strong phase  $\Theta$  associated with the strong  $CP$  problem, but it is ruled out by experiments.

an effective real valued Lagrangian of mass dimension four

$$\begin{aligned}\mathcal{L}_6 &= \frac{1}{\Lambda^2}(\alpha'_{tG}\mathcal{O}_{tG} + \alpha'^*_t\mathcal{O}_{tG}^\dagger) = \frac{1}{M^2}(\alpha_{tG}\mathcal{O}_{tG} + \alpha'^*_t\mathcal{O}_{tG}^\dagger) \\ &= \{\bar{t}_L = (P_L t)^\dagger \gamma_0 = t^\dagger P_L \gamma_0 = t^\dagger \gamma_0 P_R = \bar{t} P_R\} \\ &= \frac{v}{\sqrt{2}M^2} \bar{t} \sigma^{\mu\nu} \{\Re \alpha_{tG}(P_R + P_L) + i \Im \alpha_{tG}(P_R - P_L)\} t G_{\mu\nu},\end{aligned}\quad (3)$$

where  $\alpha_{tG}$  and  $\alpha'_t$  are the coupling constants, and  $M$  is an arbitrary mass scale since a priori we do not know the scale of new physics  $\Lambda$ . There is an explicit separation between the  $CP$ -even and  $CP$ -odd terms, and we see that the  $CP$  violating term is associated with the imaginary part of the coupling constant. Since the dynamics of the Higgs field is neglected, one can just as well regard  $\mathcal{L}_6$  as a Lagrangian built by operators of mass dimension five [56]

$$\mathcal{L}_5 = -\frac{C_5}{2} \bar{t} \sigma^{\mu\nu} t G_{\mu\nu}^a T^a - i \frac{D_5}{2} \bar{t} \sigma^{\mu\nu} \gamma_5 t G_{\mu\nu}^a T^a$$

where  $C_5$  is the chromo-magnetic dipole moment (CMDM) and  $D_5$  is the chromo-electric dipole moment (CEDM). The relations between the constants in  $\mathcal{L}_6$  and  $\mathcal{L}_5$  are

$$C_5 = -\frac{\sqrt{2}v}{M^2} \Re \alpha_{tG} \text{ and } D_5 = -\frac{\sqrt{2}v}{M^2} \Im \alpha_{tG} \quad (4)$$

The couplings  $C_5$  and  $D_5$  are not dimensionless. A practical definition of dimensionless couplings of order one ( $c_t, d_t$ ) are

$$C_5 = g_s \frac{c_t}{m_t} \text{ and } D_5 = g_s \frac{d_t}{m_t} \quad (5)$$

where  $g_s$  is the strong coupling constant. We have now accomplished what we originally set out to do: to parametrize the leading order  $CP$  violating effects in  $t\bar{t}$ -production in terms of a single dimensionless parameter  $d_t$ .

However, since the terms in  $\mathcal{L}_6$  are not renormalizable there will exist a triviality limit from the unitarity of the  $S$ -matrix. The unitarity constraint has been estimated in reference [57] to be

$$|\Re \alpha_{tG}| \simeq \frac{m_t^2 \sqrt{\pi}}{v \Lambda \sqrt{1 + \frac{2}{3} \alpha_s}}, \quad \text{for } \Lambda < 10 \text{ TeV.}$$

If we assume that  $|Re(\alpha_{tG})| \simeq |Im(\alpha_{tG})|$  and set the scale of new physics at  $\Lambda = 2$  TeV we find<sup>7</sup>

$$d_t < \mathcal{O}(1).$$

This means that if there is new physics at 2 TeV, the model  $\mathcal{L}_6$  will provide a reasonable effective description for  $d_t$  below this number.

---

<sup>7</sup>According to reference [57] there is a unique definition of the unitarity constraint if we use  $M$  instead of  $\Lambda$  as the mass scale in  $\mathcal{L}_6$ .

## 8.2 ATLAS sensitivity to an anomalous $g t \bar{t}$ vertex

The estimated cross-section for  $t\bar{t}$  production at the LHC is 833 pb [58]. Given the initial luminosity of  $10 \text{ fb}^{-1}/\text{yr/experiment}$  the ATLAS detector will have more than 8 million events per year available at its interaction vertex. Since the  $t\bar{t}$  events are quite easy to separate from the background with high efficiency, there will be a huge data sample available for precision measurements in the top sector. Assuming this sample we can ask: what is the upper limit we can put on the  $CP$  violating parameter  $d_t$ ? Before we can answer that question we must understand, that is have an accurate model for, both the production and the detection mechanisms. The production of  $t\bar{t}$  is dominated by gluon-gluon collisions at the LHC energies, where one gluon is “pulled out” of each proton. The gluon content of a proton cannot be calculated explicitly since it is a non perturbative quantity, but it has been measured and parameterized in terms of the fractional momentum ( $x$ ) of the proton carried by the gluon and the squared momentum transfer ( $Q^2$ ). The parameterizations are called parton distribution functions (PDF), see for example reference [59]. The fact that the PDF is independent of the hard process simplifies the calculations tremendously.

### 8.2.1 Event production

There was no event generator available that included the effects of  $\mathcal{L}_5$ , so a new one had to be written. The starting point for designing an event generator is the cross-section, see section 2.5 for the used formula. The dynamics is given by the squared matrix element  $|\mathcal{M}|^2$  which was calculated at tree level using the SM Feynman rules with the addition of the two Feynman rules from  $\mathcal{L}_5$

$$V_1 = -ig_s \sigma^{\mu\nu} \left( \frac{ic_t}{m_t} - \frac{d_t}{m_t} \gamma_5 \right) q_\nu T^a$$

$$V_2 = g_s^2 \sigma^{\mu\nu} \left( \frac{ic_t}{m_t} - \frac{d_t}{m_t} \gamma_5 \right) f^{abc} T^c$$

It is crucial to calculate the  $|\mathcal{M}|^2$  for the complete decay chain, since the  $CP$  violation is mediated by the spin-spin correlations between the top and anti-top quark. The spin of each quark is then reflected in the decay products due to the nature

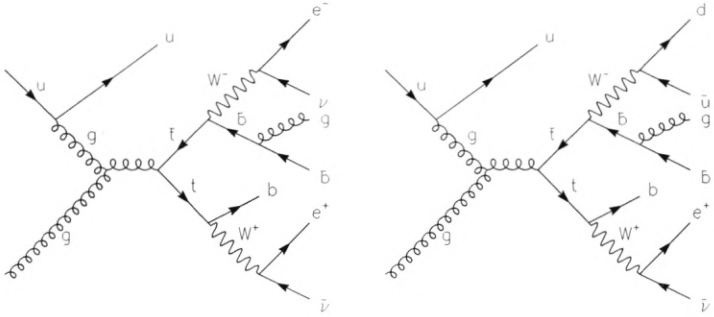


Figure 18: S-channel part of a typical dilepton (left) and lepton + jets (right) final state event including examples of initial and final state radiation handled by PYTHIA.

of the weak interaction. This means that the electron or the d-quark tend to be in the direction of the top spin in the top rest frame. Typical diagrams used in the calculations are shown in Figure 18.

There is also a factor which includes the phase-space  $\Phi_f$  which needs special treatment when there are many final state particles in order to make the sampling of the phase-space volume effective. In a proton-proton collision there are many more effects apart from the hard process that must be modeled, e.g. beam remnants, initial state radiation, final state radiation, hadronization. This was handled by interfacing the output of the hard process with the existing well tested general purpose generator PYTHIA [49]. The details of the event generator and the implementation is described in Paper III.

### 8.2.2 Analysis

The response of the ATLAS detector was modeled by an existing parameterized detector simulator ATLFAST [50]. The parameterizations are given by the design specifications, which have been verified by test-beam results (where possible) and detailed full detector simulations. ATLFAST includes the detector acceptances and an approximative description of the trigger.

The analysis consists of the standard top physics cuts for rejection of the most dangerous backgrounds, followed by a complete kinematic fit to the event. This means that all momenta of the final state particles are available for construction of effective observables for  $CP$  violation. Two final state topologies were analyzed: opposite signed leptons (dileptons), and lepton+jets, see Figure 18. The issue of which observable to use given a set of final state momenta is quite interesting. If we assume that the cross-section is perturbed by a small parameter  $\lambda$ , then the

cross-section can be expanded as

$$\sigma \simeq \sigma_0 + \lambda \sigma_\lambda,$$

where  $\sigma_0$  is the unperturbed cross-section. In our case  $\lambda$  is the  $d_t$  parameter. If we ask which observable ( $f$ ) we should use in order to maximize the signal to noise ratio it turns out that there is a unique choice, the optimal observable, which is given by [60]

$$f = \frac{\sigma_\lambda}{\sigma_0}.$$

This is very useful as a guide or as a benchmark in the process of finding the most suitable observable that is both efficient in terms of the signal to noise ratio and robust against systematic errors. The observable used in the analysis is the asymmetry

$$f_2(l^+, l^-, b, \bar{b}) = \frac{\epsilon_{\mu\nu\sigma\rho} p_{l^+}^\mu p_{l^-}^\nu p_b^\sigma p_{\bar{b}}^\rho}{(p_{l^+} \cdot p_{l^-} - p_b \cdot p_{\bar{b}})^{1/2}}$$

which has been estimated in the literature to be about five times less effective than the optimal one. There is big advantage of using an asymmetry since the systematic effects do not contribute to first order. In practice this means that the results are not very sensitive to absolute errors in the energy scale, uncertainties in the PDF and higher loop corrections (K-factors).

One might worry about the level of contamination in the observable from  $CP$ -even processes. That this is under control is demonstrated in a clear and understandable way in reference [61]. The differential cross-section can be written as

$$d\sigma = 2f_a^p(x_1)f_{\bar{a}}^p(x_2)d\hat{\sigma}(a\bar{a} \rightarrow t\bar{t})dx_1dx_2,$$

where  $f_a^p$  is the PDF for particle  $a$ , and  $d\hat{\sigma}$  is any  $CP$ -even tree level process that produces  $a\bar{a} \rightarrow t\bar{t}$ . We can then split the PDF part into  $CP$ -even ( $F^+$ ) and  $CP$ -odd ( $F^-$ ) contributions

$$2f_a^p(x_1)f_{\bar{a}}^p(x_2) = F^+ + F^-,$$

where

$$\begin{aligned} F^+ &= [f_a^p(x_1)f_{\bar{a}}^p(x_2) + f_a^p(x_2)f_{\bar{a}}^p(x_1)], \\ F^- &= [f_a^p(x_1)f_{\bar{a}}^p(x_2) - f_a^p(x_2)f_{\bar{a}}^p(x_1)]. \end{aligned}$$

Since  $F^+$  is  $CP$ -even it cannot contribute. The term  $F^-$  however, is  $CP$ -odd and may contribute. If we let  $a = g$  we immediately see that gluons cannot contribute at tree level to the contamination. Any contamination must arise from initial quarks. Another conclusion that can be drawn is that Lorentz invariant observables cannot receive any contributions either. This is because  $F^- = F^-(x_1, x_2)$  and Lorentz invariant quantities can only be proportional to  $x_1x_2$ . This means that we can always find a frame such that  $F^- = 0$ . For more details concerning the analysis please see Paper IV.

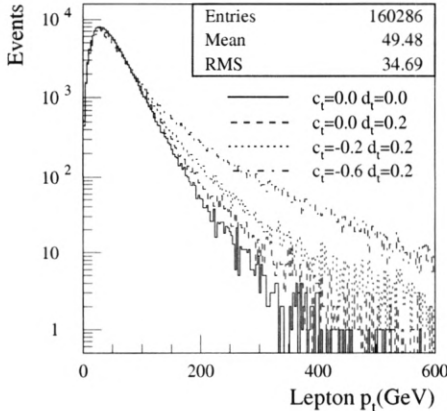


Figure 19: Lepton transverse momentum spectra. The tail of the spectrum is very sensitive to  $CP$ -even effects in the  $g t \bar{t}$  vertex. The  $(-0.6, 0.2)$  point of no sensitivity for  $CP$  violation can clearly be ruled out by this simple measurement. Also the small effects of quadratic  $d_t$  terms in  $(0, 0.2)$  is seen.

### 8.2.3 Results

The result from the analysis is an expected experimental upper limit for the  $d_t$  parameter after one year of running at low luminosity. Under the condition that the  $c_t$  parameter is small the estimated ATLAS limit is

$$d_t < 0.05.$$

Both the dilepton and lepton + jets channels are independently capable of achieving this result. The requirement of a small  $c_t$  parameter comes from the observation that there is a region where the sensitivity is reduced, or even canceled (e.g.  $c_t = -0.6$ ,  $d_t = 0.2$ ). However, since the part controlled by  $c_t$  is a  $CP$ -even quantity, there are many strong observables available to provide independent constraints. An example of this is the deviation from the SM lepton transverse momentum spectrum, see Figure 19. The current limits on  $d_t$  and  $c_t$  comes from the top pair production cross-section at the Tevatron. The  $d_t$  limit given in reference [56] is

$$d_t < \mathcal{O}(1).$$

The experimental limit is not sensitive to the predictions of the most probable specific models. For example multiple Higgs doublet models [62] predict

$$d_t \simeq 0.001.$$

However, the experimental limit is still interesting in itself since it provides a model independent measurement of a fundamental symmetry.

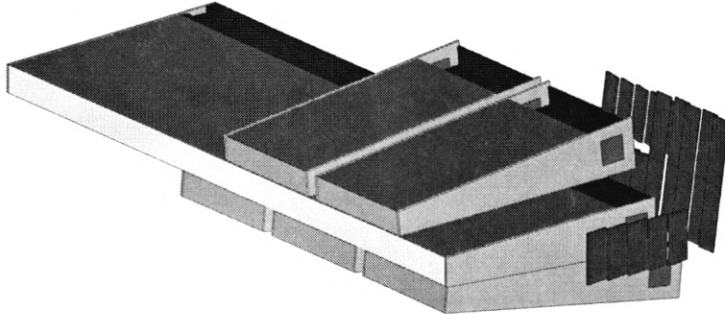


Figure 20: Setup of the barrel module 0 test-beam in 1996 and 1998.

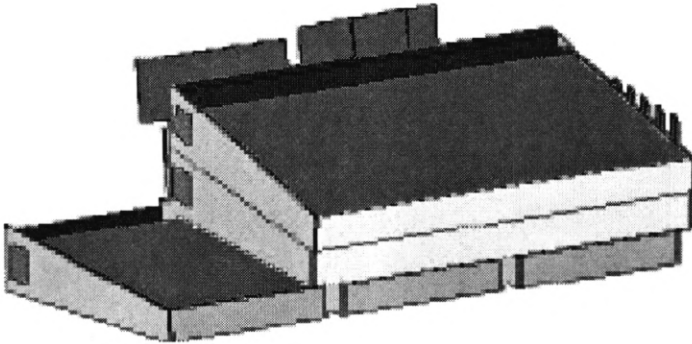


Figure 21: Setup of the extended barrel module 0 test-beam in 1997.

## 9 TileCal test-beam

The test-beam program at CERN for the Tile calorimeter started in 1993 as RD34. During the last years tests have been performed at the north area in Prevessin using protons extracted through the H8 beam line from the SPS. The proton beam is converted into muons, electrons and pions in the energy range 10 GeV to 400 GeV and focused on the calorimeter at different angles. The program covers all aspects of the calorimeter: mechanics, optics and electronics. The tests of modules with real ATLAS geometry started in 1996 with the barrel module 0. The 1 m prototype modules from 1995 test-beam are used to measure the lateral leakage. Also visible are the scintillators used as "muon walls". The extended barrel module 0 was tested in 1997, see Figure 21.

The analysis of test-beam data is done from ntuples produced by an offline version of the online monitoring program TileMon [64]. During data taking raw data is stored on disk in the ZEBRA format [65]. After the run is finished data is

transferred to tape for later retrieval. With TileMon many reconstruction features are controlled by data cards, but the user can also intercept the ntuple creating chain with C or fortran code.

Since the author's contribution concerns the calibration and evaluation of the 1996-1998 fast readout electronics the following sections will, after an introduction to the signal processing of the charge from the photo-multiplier tubes, give a historical overview of its development and performance. An overview of the readout and its requirements are given in sections 5.2.3 and 5.3.

## 9.1 Charge reconstruction

The shaped pulse from the 3-in-1 card is sampled by an ADC every 25 ns. During ATLAS operation a frame of at least 5 samples of the pulse will be available. A few samples before each frame will also be available to estimate the average bias or "pedestal". One must be aware of the fact that the actual procedure used for reconstruction of the charge from the ADC samples will affect both the absolute calibration and the resolution for real data. What the optimal procedure is depends crucially on the transfer function of the system.

If the analog system is linear in  $Q$  and has a bandwidth much larger than the signal in the entire dynamical range, then there exists a well known optimal method to estimate the charge. This method is called the optimal filter and is anticipated to be the method used in ATLAS. Another and more explicit way to state the conditions is to say that the system response  $S(t, Q)$  to a charge  $Q$  must be shape invariant, i.e. there exists a function  $s(t)$  such that  $S(t, Q) = Qs(t)$ . The function  $s(t)$  is the output pulse shape normalized to 1. All contributions to the charge resolution are optimally minimized by the optimal filter, i.e. pile-up noise, electrical noise, quantization noise and time jitter. Especially in test-beam time jitter is a problem since the sample-and-hold is uncorrelated with the trigger. The optimized quantities in the time domain to first order [22] are

$$Q^* = \sum_i a_i S_i, \quad (6)$$

$$Q^* \tau^* = \sum_i b_i S_i, \quad (7)$$

$$(8)$$

where

$$S_i = LUT(ADC_i - P) = Qs(t_i - \tau) + n_i \simeq Qs_i - Q\tau \frac{ds_i}{dt_i} + n_i. \quad (9)$$

The constraints are

$$\langle Q^* \rangle = Q, \quad (10)$$

$$\langle Q^* \tau^* \rangle = Q\tau, \quad (11)$$

$$\min_{a_i} \sum_{ij} a_i a_j \langle n_i n_j \rangle, \quad (12)$$

$$\min_{b_i} \sum_{ij} b_i b_j \langle n_i n_j \rangle. \quad (13)$$

$ADC_i$  is the ADC sample at time  $t_i - \tau$  and  $P$  is the pedestal at the ADC input. The function  $LUT()$  normalizes  $S(t)$  such that  $\max S(t) = Q$ . The function  $LUT()$  can also be used to linearize the system response. This is described later in this chapter. The discrete version of the shaper function  $s_i$ , is defined in such a way that there exists an  $i$  such that  $s_i = 1$ , i.e. one of the time samples is the peak time sample. Note that  $S_i$  and  $ADC_i$  are not required to exist at the same time as  $s_i$ , the allowed difference is the phase factor  $\tau$  which represents the time between the true peak time and time of the maximal sample. The time step in  $i$  is in this case 25 ns. The stochastic process  $n_i$  models the noise on top of the average pedestal level. The correlation  $\langle n_i n_j \rangle$  can be estimated from pedestal runs, i.e. samples without signal. Note how much the power of the optimal filter is based on the condition that  $s_i$  is independent of  $Q$ . Hence this is a basic requirement on the fast readout electronics.

### 9.1.1 Pulse shape reconstruction

The pulse shape  $s_i$  is trivially estimated from the measured quantities  $S_i$  and the known injected charge  $Q$ . During charge injection it is possible to scan  $t$  in steps of 0.185 ns and hence  $i$  is a very good approximation of continuous time. Consequently  $S_i = Q s_i$  and we have

$$\frac{\partial S_i}{\partial Q} = s_i \quad (14)$$

However due to imperfections in the injector system there are contributions from leakage in the capacitor switch which can be modeled as  $l(t)$  and a compensating constant charge bias  $b$ . So if  $Q'$  is the charge set in the hardware, the true charge  $Q = Q' + b$ . We now have

$$S_i = (Q' + b)s_i + l_i = Qs_i + l_i \quad (15)$$

but equation (14) remains the same.

### 9.1.2 Readout linearization

Due to the advanced injector system, the intrinsic hardware is not required to be linear. By mapping each ADC count to the correct charge  $Q$  it is straightforward to linearize the response. The mapping is called a look-up-table (LUT). However, just as in the optimal filter case, the pulse must be shape invariant or equivalently

$\partial s_i / \partial Q = 0$ . Otherwise the mapping will not be unique and additional information beyond  $S_i$  is needed to lift the degeneracy. The mapping is then simply a modified version of equation (15)

$$S_i = LUT(ADC_i - P) = Qs_i + l_i = \{\text{at the pulse peak}\} = Q' - Q_0 \quad (16)$$

$Q_0$  is found by linear extrapolation to  $S_i = 0$  assuming the system to be linear at small signals. The linearization can in principle be made at any instant of time as long as there is signal, but if it is not performed at the pulse peak the absolute  $Q$  will not be correct. The absolute scale can in that case be calibrated by an extra constant ( $C$ ) included in the optimal filter, i.e.

$$Q^* = C \sum_i a_i S_i \quad (17)$$

Please note that the dominating noise must enter before the non linearities in order to fulfill the optimal filter conditions.

It is possible to map any function  $Q^* = f(S_1, S_2, \dots, S_n) = Q' - Q_0$  for an arbitrary system as long as it is bijective, but then we have left the idea of linear optimal filtering. That this is not acceptable is probably one of the most important conclusions in this paper as we will see later on in the evaluations of the test-beam results. This is of course not true if one can prove that the new configuration is as effective and robust as the linear optimal filter, but that is extremely difficult. E.g. a priori, the true ATLAS noise correlations are unknown.

## 9.2 The concept of non linear compression, test-beam 1994

A 16 bit Analog to Digital Converter (ADC) capable of a 40 MHz sampling rate was not available, especially not considering the constraints set by the economy and power consumption of the  $10^4$  readout channels. However, since the calorimeter resolution scales as  $\sqrt{E}$  one is led to redistribute the ADC resolution, i.e. signal compression.

The FERMI-project[66] (CERN RD-16) had developed a complete concept to handle the readout from LHC-type calorimeters. Hence FERMI had available a compressor and a 10 bit ADC that could be matched exactly to the requirements of the hadronic and electromagnetic calorimeters. Test-beams during 1994 showed that this was a possible way to go, at least for Tilecal assuming modest bandwidth and slew-rate demands. With two working readout channels, a 0.66% resolution for large signals and stable pedestals were demonstrated with the 200 ns FWHM Tile shaper. For a detailed report see [67].

## 9.3 A comparative test of non linear compression, test-beam 1995

To demonstrate the operation of the compressor concept, 27 FERMI channels were compared with the standard readout during test-beam 1995 with the 1 m Tilecal

### Small Signal Frequency Response for Analog ASIC in 68 pin PLCC as Measured on CAEN V571

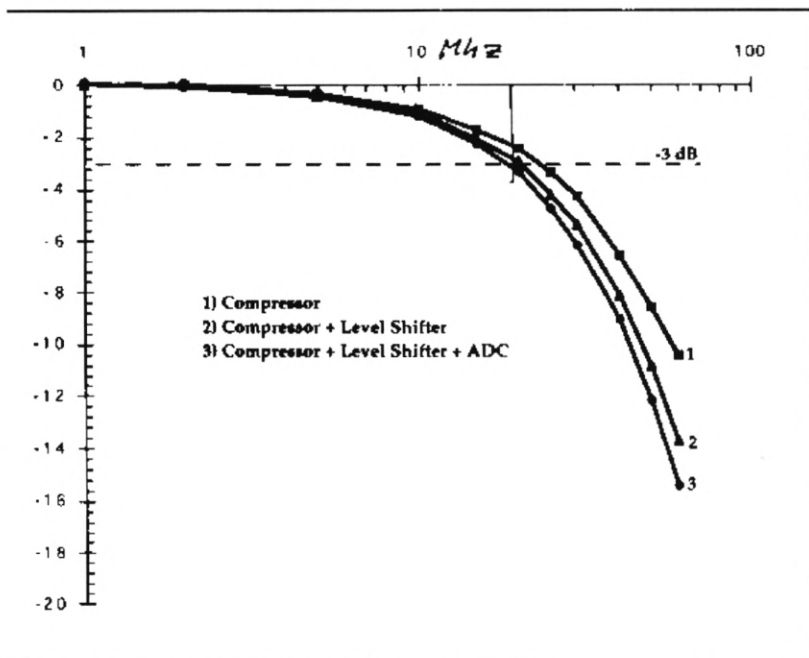


Figure 22: Measured bandwidth of the compressor located on the VME board during 1995.

prototype modules. The limited bandwidth of the compressor made it impossible to use the 50 ns shaper aimed for in the final design, see Figure 22. In order for the test-beam work to progress a temporary 200 ns shaper was implemented. However, even with such a wide pulse a tendency to slew-rate was detected during the critical look-up-table construction. Apart from the slew-rate, the compressor solution performed as expected, see [68] for details.

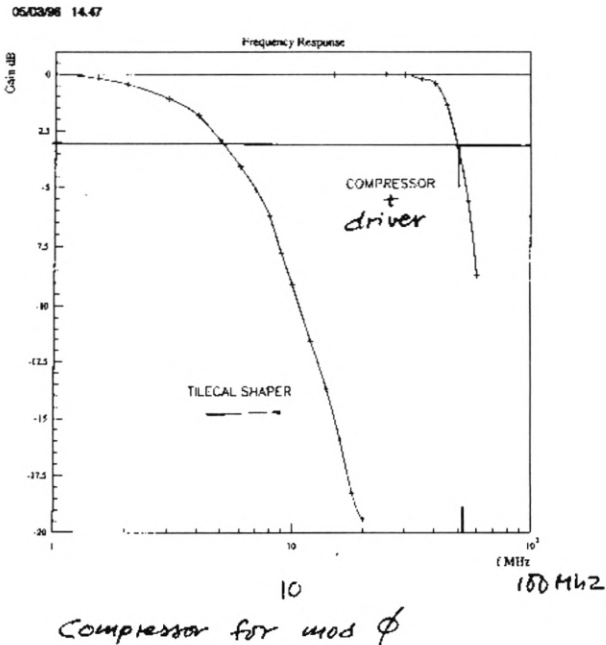


Figure 23: Measured bandwidth of the shaper and the compressor [69] implemented in the process Genum Ga 911 located on the 3-in-1 card during 1996.

## 9.4 Approaching realistic ATLAS requirements, test-beam 1996

During 1996 test-beam, 46 channels with FERMI modules were used for the readout of the Tile calorimeter barrel module 0. The most important changes of the fast electronics were a realistic shaper with a FWHM of 50 ns, a new integrated charge injector and a new and faster compressor, see Figure 23. All this functionality was located on the 3-in-1 card. The sampling 10 bit FERMI ADCs were mounted in VME crates with 3 ADC's per VME card.

### 9.4.1 Pedestal analysis

Measurements of the pedestal, that is the base line without signal, are extremely important. The pedestal contains information about the noise in the system. The noise can in most cases be approximated by a weak stationary process  $X_i$  and

as such it is characterized by the mean  $E(X_i) = P$  and the covariance<sup>8</sup> kernel  $R(j) = \text{Cov}(X(i), X(i+j))$ . Both these quantities can easily be measured from a pedestal run. For a comparison with the variables in the optimal filter let  $X_i = n_i + P$ . The electronic noise is constrained by the requirement to resolve muons in the first and thinnest compartment where the Landau peak is at  $\sim 350$  MeV and should be sampled at an ADC level of 11 counts for good resolution. The Landau tail stretches down to  $\sim 100$  MeV. The compartment is seen by two PTMs, consequently the intrinsic noise from the electronics should be sufficiently lower than  $\sim 70$  MeV/channel to separate the muon signal from the pedestal. During 1996 the charge calibration gave  $\sim 0.017$  pC per ADC count and the electromagnetic scale from electrons gave  $1.37$  GeV/pC. Thus the pedestal noise should be much lower than 3 ADC counts. One notes that the gain is a little bit too low (7.5) for the requirement of 11 counts for muons. The pedestal widths for 1996 are shown in Figure 24. We see that the mean of the distribution is  $\sim 2.5$  ADC counts and has an unpleasant upper tail. There is no real reason to expect the channels to be more noisy than the 1995 values of 1 ADC count. By inspecting the correlations of the pedestal it is clear that a large part of the noise is correlated, see Figure 25. The noise is clearly external and probably related to a digital clock. When using exactly the same 10 bits ADCs in a completely different configuration during 1998, large correlations were observed for the 10 bits ADC cards. Hence the 10 bits ADC cards contribute to the correlated noise. The exact origin of the remaining contributions was never established. Another aspect of the pedestal is related to the fact that the system is AC coupled. Due to the AC coupling the mean pedestal level will depend upon the integral of the signal per time interval. Since the pulse is unipolar, or positive, the net integral is positive. Hence the pedestal must be estimated on an event to event basis. An increased pedestal level was e.g. clearly seen during charge injection runs when the interval between injections was set very tight, see Figure 26.

#### 9.4.2 Pulse shape invariance

The requirement of shape invariance, i.e.  $S(t, Q) = Qs(t)$ , is very strong. E.g. the requirement of linearity is just a subrequirement which is quite explicit at the pulse peak where  $S(t_{peak}, Q) = Q$ . So the next property to check after evaluating the pedestals is the shape invariance. In order to reconstruct the pulse shape a handle on the phase between the pulse and the trigger is needed. Unfortunately the injector phase was not properly stored during data taking so some other method had to be used. There exists a time to digital converter in all test-beam setups, but it is not available during charge injection. One practical way to estimate the phase difference  $\tau$  is to use the samples themselves. Since the pulse is smooth and nearly symmetric,

---

<sup>8</sup>The covariance between  $a$  and  $b$  is defined as  $\text{Cov}[a, b] = <(a - \bar{a})(b - \bar{b})>$ , and the correlation coefficient  $\rho$  is defined as  $\rho = \text{Cov}[a, b]/\sqrt{\text{Cov}[a, a]\text{Cov}[b, b]}$ .

07/04/98 23.26

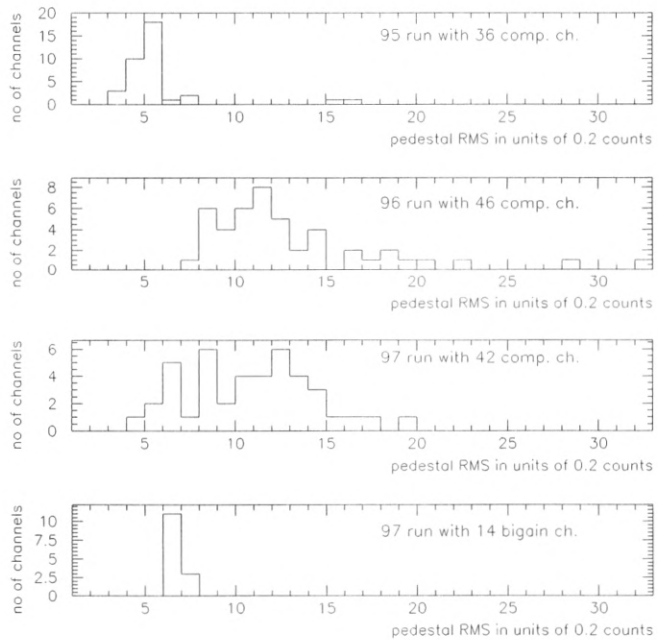


Figure 24: Distributions of the RMS pedestal widths for the test-beam periods 1995 to 1997.

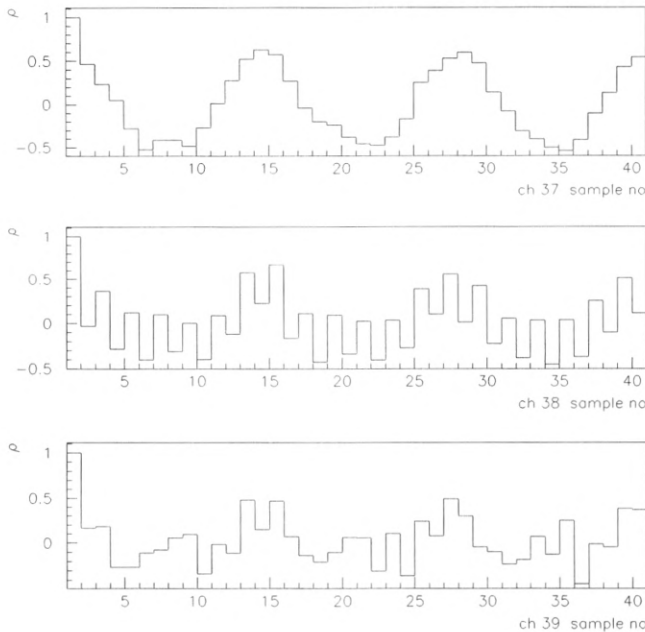


Figure 25: Large unexpected correlations seen between samples within the same frame taken from 1996 pedestals. The source was unknown at this point but later part of the correlation could be traced to the 10 bits FERMI ADC boards.

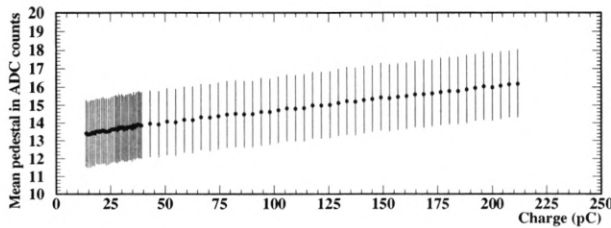


Figure 26: Pedestal drift during 1996 charge injection due to the unipolar shaping and AC-coupling. The error bars are the event to event spread for one pedestal sample and do not represent the error of the mean.

the so called slope [70] is a good choice. The slope is defined as

$$\text{slope} = \frac{ADC'_{max+1} - ADC'_{max-1}}{ADC'_{max}} \quad (18)$$

where  $ADC'_{max+1}$  means the pedestal corrected ADC sample one sample after the maximum ADC sample. That this is reasonable is clear after Taylor expansion of the response function  $f(t)$  equals the time of the true peak maximum)

$$ADC'_{max+1} = f(t + \Delta + \tau) \simeq f(t + \Delta) + \tau f'(t + \Delta) \quad (19)$$

$$ADC'_{max-1} = f(t - \Delta + \tau) \simeq f(t - \Delta) + \tau f'(t - \Delta) \quad (20)$$

$$ADC'_{max} = f(t + \tau) \simeq f(t) + \tau f'(t) \quad (21)$$

where  $\Delta$  is the time between samples, i.e. in this case 25 ns. We finally get

$$\text{slope} \simeq \frac{f(t + \Delta) - f(t - \Delta) + \tau(f'(t + \Delta) - f'(t - \Delta))}{f(t) + \tau f'(t)}. \quad (22)$$

Assuming a smooth and symmetric pulse we get a sensitive estimator at  $\max_{\Delta} |f'(t + \Delta)|$ . Since  $f'(t) = 0$  we have

$$\text{slope} \simeq \frac{2\tau f'(t + \Delta)}{f(t)}. \quad (23)$$

However, the mapping of slope to time is not required to be linear. It is enough if it is bijective. Since the random phase distribution in time is flat, a linear time is simply found by rebinning the slope distribution such that an equal number of events is found in each time bin, see Figure 27.

Given the phase estimator it is straightforward to reconstruct the pulse shape. For a one channel example of the 62 available amplitudes see the top plot in Figure 28. In order to study the shape invariance, the raw compressed pulses must be linearized. To get the absolute scale correct the charge offset  $Q_0$  must be extracted by extrapolation to  $S(t) = 0$ , see Figure 29. Now the linearization and the construction of the LUT can be performed by applying equation 16. For an example of a LUT see the top plot in Figure 30. Given the LUT it is possible to check the intrinsic quantization resolution of the system given an ideal ADC. Propagation of error yields

$$\sigma_Q = \frac{\partial \text{LUT}(ADC)}{\partial ADC} \sigma_{ADC}. \quad (24)$$

For  $\sigma_{ADC}$  one can assume a flat distribution, hence  $\sigma_{ADC} = 1/\sqrt{12}$  counts. For an example see the bottom plot in Figure 30. A comparison is also made to the intrinsic resolution of the calorimeter, and we see that by design we are on the safe side concerning the theoretical quantization noise<sup>9</sup>. After LUT expansion we see already by eye in the lower plot in Figure 28 that the shape invariance is far from conforming

---

<sup>9</sup>It is in place here to notice that since the quantization noise enters after the compression it is not properly handled by the optimal filter.

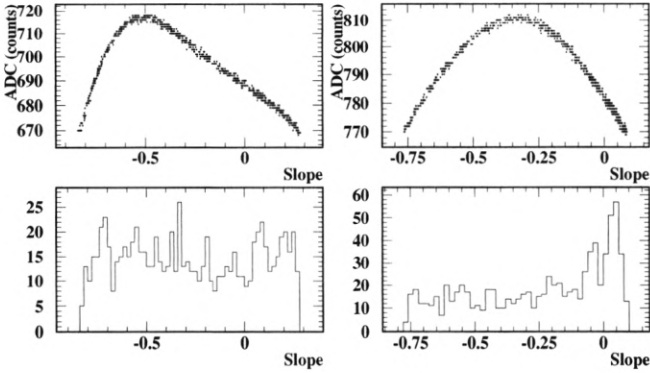


Figure 27: Examples of slope distributions from 1996 charge injection data. Since the phase distribution in linear time is flat, knowledge of slope distribution enables construction of a linear time estimator.

to the 1% requirement. We know by now that this means that the optimal filter will not work, and also, that the LUT(ADC) is not a valid linearization. This is of course very bad. The reason for the bad shape invariance is clearly insufficient slew-rate in the analog chain, the most striking feature being the timewalk of the peak position clearly visible by eye in the expanded pulse plot. One other important aspect concerning the requirements is seen in the example of the LUT in Figure 30. It saturates already at 200 pC, while the requirement says 800 pC! Due to the pedestal the real saturation is even lower than 200 pC and the spread of this saturation among the channels ranges from 100 to 190 pC. By design the charge injector in the 1996 version of the 3-in-1 handled only up to 400 pC, however due to an error in the matching to the ADC, saturation sets in far too early. Great care had to be taken during the analysis, e.g. for the investigation of 400 GeV pions.

#### 9.4.3 Charge estimator resolution

It is impossible to speak about resolution without at the same time mentioning the method for charge reconstruction. Assume for a moment that we had a square pulse shape 5 samples long without time jitter and that the pedestal noise is orthogonal. Then the resolution of an unweighted sum of 5 signal samples<sup>10</sup> would be  $\sqrt{5}/5$  times the one sample estimator. Now, first of all, the Tile shaper is not a square but tries to mimic a Gaussian. The Gaussian is the unique solution to the problem of finding a pulse that is as short as possible both in the time and in the frequency

---

<sup>10</sup>This is actually the optimal filter for this configuration

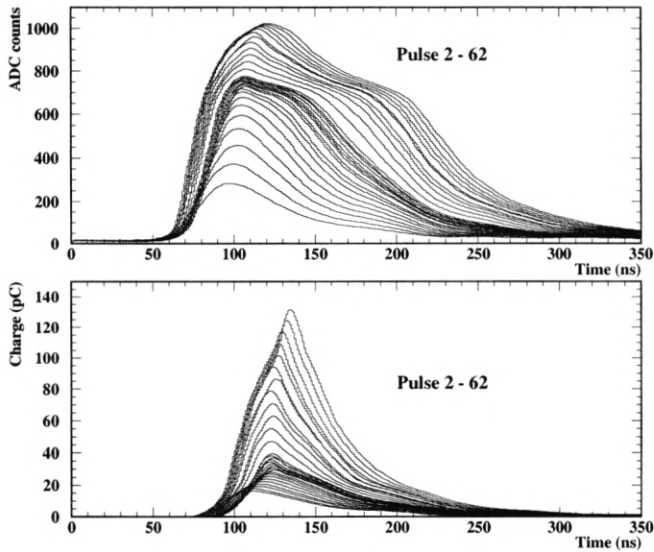


Figure 28: Examples of the compressed (top) and  $LUT(ADC_i - P)$  decompressed pulses (bottom) reconstructed from one channel in charge injection runs during 1996.

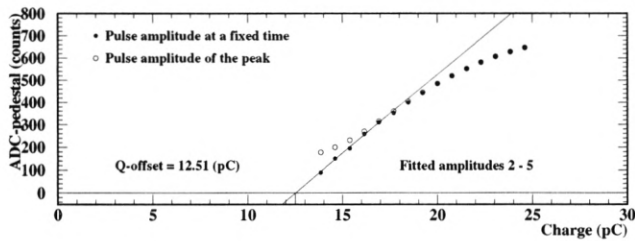


Figure 29: Extrapolation of the charge offset  $Q_0$  at  $S(t) = 0$ .

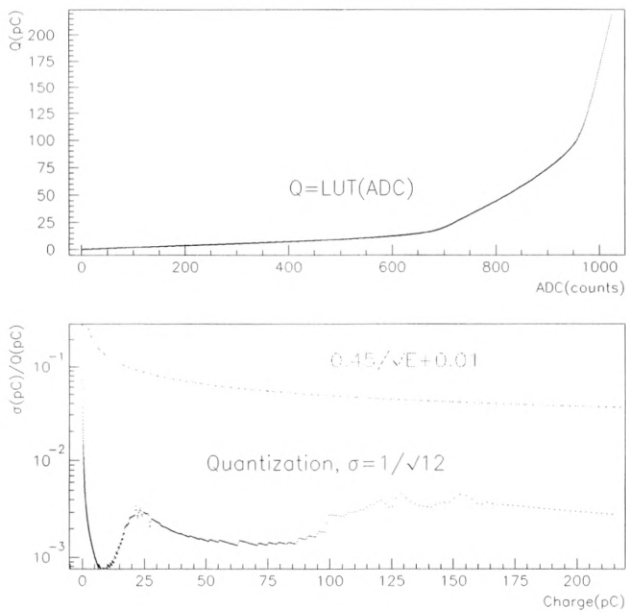


Figure 30: Example of a LUT from 1996 (top). Given the LUT (top) an estimation of the quantization noise assuming an ideal ADC is shown (bottom). Included is also a comparison to the intrinsic calorimeter resolution.

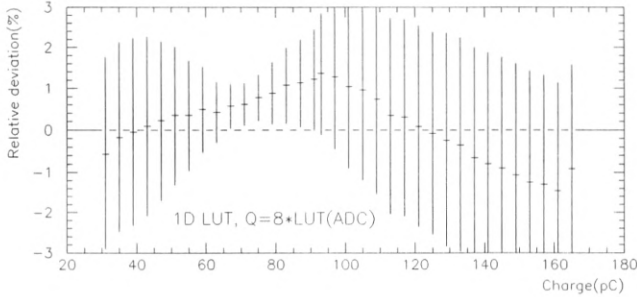


Figure 31: One channel example of the relative deviation with the 1D LUT in 1996. The estimator is an unweighted sum of 8 linearized ADC samples. Both the linearity and the resolution is visible in the plot. The resolution is the height of the error bars.

domain, this is highly desirable. Given the pulse shape we know how to construct the optimal filter estimator. Unfortunately we see in Figure 28 that the pulse is not invariant and the optimal filter is no longer an option. One would expect that the unweighted sum is not so far from optimum, but we see in Figure 31 that the resolution and linearity is so bad that it is almost meaningless to perform basic test-beam physics analysis.

In order to save the test-beam analysis, some alternative method had to be invented with the only requirement to perform well enough under test-beam conditions. Many different configurations were tested. Finally the method that was most effective was to first add samples of the compressed pulse and then linearize. The optimal number of samples was 8. The compressed sum was still phase dependent but that could be remedied by a slope correction. So in the end, the new method had the structure of a nonlinear 2 dimensional (2D) mapping

$$Q = \text{LUT}(\max_{i_0} \sum_{i=i_0}^{i_0+7} \text{ADC}'_i, \text{slope}) \quad (25)$$

It was implemented as a grid with 127 bins in amplitude and 150 bins in phase. The amplitude used spline interpolation, while the slope used linear interpolation. As we can see in Figure 32, the resolution is below 0.5% and the linearity is by construction better than 1%.

In the normal case one would keep the frame of samples fixed in time. However, the peak position was not stable in the hardware. Since the LUT is critically dependent on the slope, the definition of slope was set at the center of the maximal sample sum which is easy to find independently of sample shifts. The problem associated

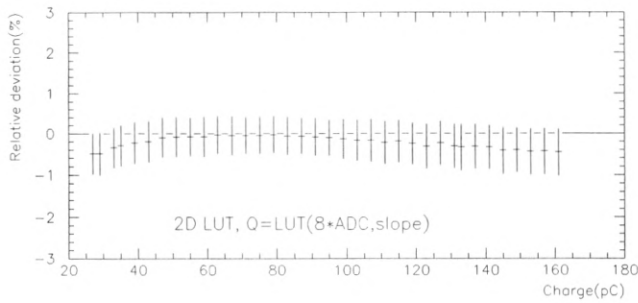


Figure 32: One channel example of the relative deviation with the 2D LUT in 1996.

with the maximization is that the estimator picks up a noise dependent bias. This was solved with a fixed sum for small signals where the slope parameter was useless anyway.

## 9.5 Second iteration and the bigain backup solution, test-beam 1997

In the 1997 test-beam<sup>11</sup> setup, two extended barrels were under scrutiny. One module (ANL) was equipped with 28 channels using 10 bit ADCs with nonlinear compression. The other one (BNL) had 14 channels of 12 bit commercial ADCs with bigain compression (cells A14-A16, B13-B15 and D7), and 14 channels of the same type as in the ANL module. The 12 bit bigain was developed as a backup solution since clearly the nonlinear compressor design had problems both in performance and robustness. The bigain compression concept is very simple. There is one channel with high gain for small signals, and one channel with low gain for large signals. If the high gain channel saturates, only the low gain channel is used. During 1997 the gain difference between low and high was 16. The drawback with the bigain solution is that the matching to the calorimeter resolution is not optimal and it is more expensive since the number of readout channels has to be doubled. However, it is linear by design. The bigain 3-in-1 also had a new passive shaper. The 3-in-1 charge injector had an increased theoretical capacity of 640 pC but was only linear up to 400 pC.

The compressor was patched in order to improve the slew-rate. It used only the positive side of the differential output since this was observed to be faster than the negative side. Concerns were raised that this would influence the noise in a negative way. But we can see from Figure 24 and 33 that the noise in the compressor channels are dominated by the correlated noise in a very similar way as in 1996. Once the correlated noise is removed, e.g. in the 12 bits channels, we are back to the same noise level as in 1995. The performance for small signals with the default implementation of the 2D LUT estimator is shown in Figure 34. The top plot shows the muon signal compared to the pedestal width in a compressor cell in the ANL module. The bottom plot shows the same thing but for a bigain cell in the BNL module. The algorithm for the fit of a Landau distribution convoluted with a Gaussian to the muon signal is due to [71]. In Figure 34, the Landau peak is a little bit too high to match the requirement, but we see a better muon separation in the 12 bits bigain system than in the 10 bits compressor system. During 1997 the conversion between charge and energy was 1.26 GeV/pC. We can also notice that for these two cells the inter-calibration was not very good.

### 9.5.1 Compressor: pulse shape invariance

The compressor had been modified since the 1997 test-beam in order to improve the shape invariance. The measurable results of the improvements are shown in Figure 35. Clearly it is a lot better than in 1996 but unfortunately the deviations are larger than 1% over the full dynamic range.

---

<sup>11</sup>From analysis point of view the most memorable problem during this period concerned cross talk between the fibers within the same "transparent" profile.

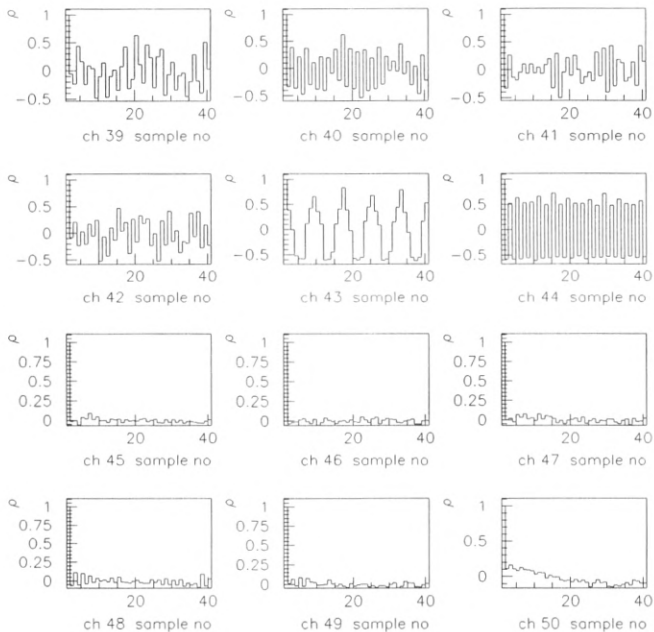


Figure 33: Correlations between samples within the same frame. Channels 39-44 are compressor 3-in-1s, and channels 45-50 are bigain 3-in-1s. In channels 45-49 the noise is very close to the definition of orthogonal noise. The presence of correlated noise only says something about the overall noise immunity of the system. Clearly in channels 45-49 the one sample pedestal spread is a good estimator of the internal noise.

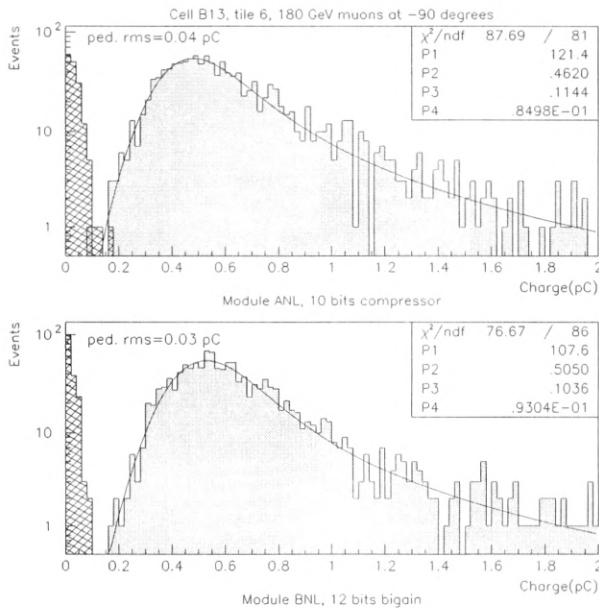


Figure 34: The 180 GeV muon signal in cell B13 is compared to the pedestal width for a cell read out with compressor electronics (top) in the ANL module. The bottom plot shows the same thing but for a bigain cell in the BNL module. The Landau peak is a little bit too high to match the requirement, but we see a better muon separation in the 12 bits bigain system than in the 10 bits compressor system. According to [71] the most probable value  $MOP = P_2 - 0.13P_3$ , and the Gaussian contribution is parameterized by  $\sigma = P_4$ .

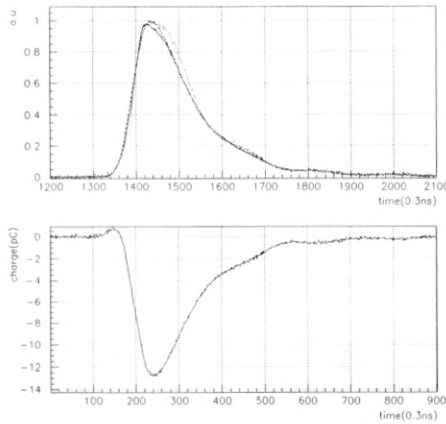


Figure 35: In the top plot the shape invariance of  $s(t)$  is shown for small, medium and large signals for a typical compressed channel during 1997. The bottom plot shows the bias and leakage ( $b + l_i$ ) for the same channel which is nearly identical to the ones reconstructed in 1996.

### 9.5.2 Compressor: charge estimator resolution

An attempt was made to apply optimal filters. The shape invariance was not good enough over the full dynamic range so the different filters were created in different regions where the shape appeared to be invariant. However, we see in Figure 36 that the performance once the LUT corrected non linearities set in ( $\sim 27$  pC) is not acceptable. Just as in 1996 the best performance was achieved with the 2D LUT technique, see Figure 37. Note that the dynamical range increased from  $\sim 150$  pC in 1996 to 400 pC in 1997.

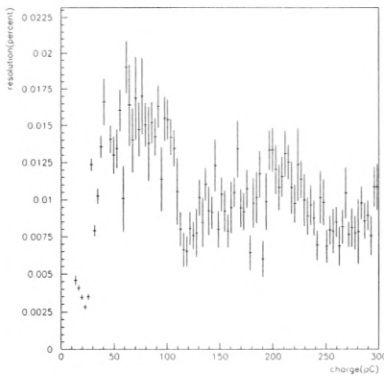


Figure 36: Charge resolution achieved with optimal filters using 1997 compressor data. Due to the pulse distortions different filters are applied in the regions [0,27], [27,55], [55,100] and [100,190] pC. Note how well the filter behaves in the undistorted and linear region below 27 pC. The Y-axis shows the relative resolution in absolute numbers, not percent (an error in the Y axis label).

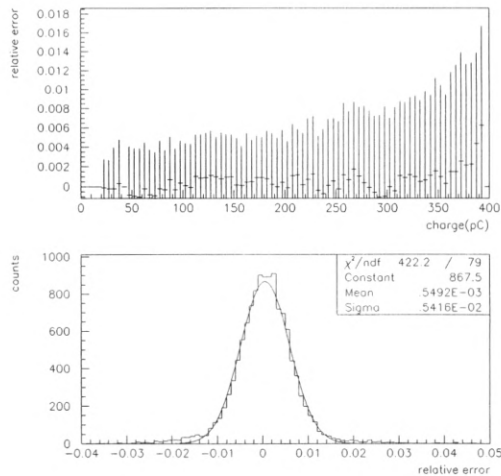


Figure 37: One channel example of the relative error for the 2D LUT estimator during 1997. The error bars represent the resolution. The bottom plot shows the projection of the relative error. From the RMS we see the that resolution is of the order 0.54%.

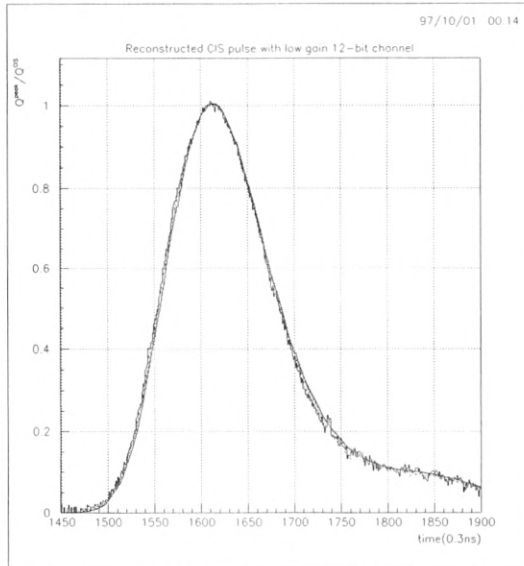


Figure 38: Shape invariance of  $s(t)$  for the passive shaper in the bigain 3-in-1 from 1997 low gain charge injection data. A small and a very large pulse are superimposed.

### 9.5.3 Bigain: pulse shape invariance and resolution

The bigain system had a new passive shaper. Early studies as soon as charge injection data was available indicated superior shape invariance of the system, see Figure 38, and a resolution with an unweighted sample sum in the 0.1% range for large signals. The bigain system was evaluated in detail by Eftymiopoulos and Kontos [72]. They demonstrated a linearity and resolution for large signals below 0.5% using only an unweighted sum of 5 samples. Note that no linearization is needed! At this point it was clear that the compressor concept was out of the game and a decision was taken to go for the bigain solution from now on. The compressor simply had too many unsolved problems. Beside the ones mentioned, one problem concerned the fluctuations in the AC coupled pedestal levels on each side of the non linear component, an obvious nightmare for calibration in the presence of pile-up noise. However, one question remained for the fast readout: could the bigain 12 bit ADC be replaced by a 10 bit ADC?

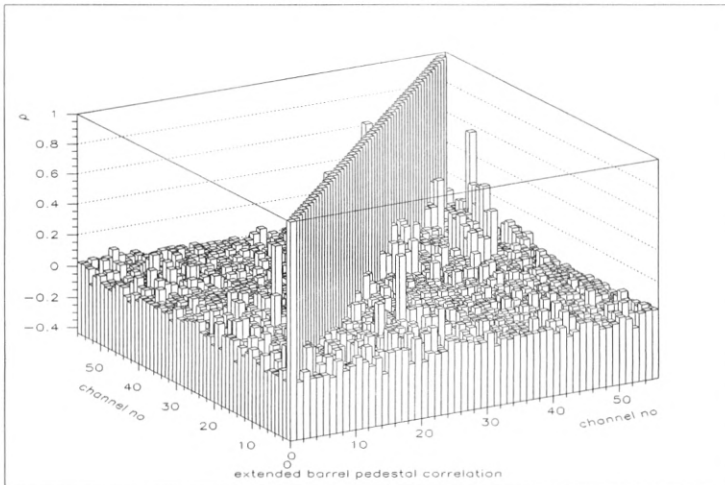


Figure 39: Correlations between the channels in the BNL extended barrel module 0. A channels is 100% correlated with itself thus the diagonal is 1. Channel 33-38, 45-50 and 55-56 are 12 bits bigain. The matrix is symmetric. Unfortunately negative correlations are not visible in the 3D plot. Both 10 bits and 12 bits channels show a correlated behavior. The cluster in the upper right corner is actually 12 bits ADCs. The level of the correlated noise is so low so that it should not affect the results from the test-beam analysis.

#### 9.5.4 Global correlations

A global property of the electronics that needs to be kept low is the correlations between channels. There are two aspects of this, noise correlations, and signal correlations. Both can be very dangerous when physical objects e.g. jets are constructed from a large collection of channels. The electronic cross-talk could e.g. be tested by injecting charge channel by channel and look for correlations in other channels. This was not tested since all channels in the setup were injected at the same time in order to reduce the overall time of the calibration procedure. However the noise correlations between the channels can be measured from a pedestal run and an example is shown in Figure 39.

### 9.6 10 bit or 12 bit ADC for bigain compression, test-beam 1998

In 1998 module 0 was tested again with 45 PMTs connected to bigain 3-in-1 cards. The 3-in-1 card had a new improved shaper and a new injector capable of 800 pC with low leakage. The gain ratio between low and high gain was increased to 64 compared to 16 during 1997 in order to cover the same dynamic range with 10 bit

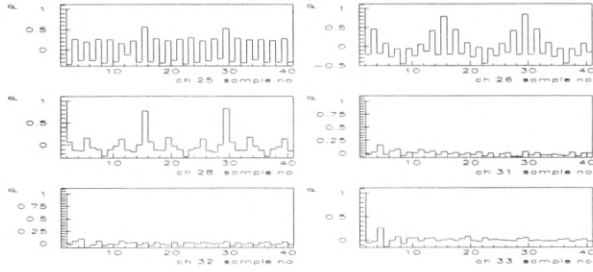


Figure 40: Sample correlations for low gain channels during 1998. The channels 25, 26 and 28 show 10 bits ADCs and the channels 31, 32 and 33 show 12 bits ADCs.

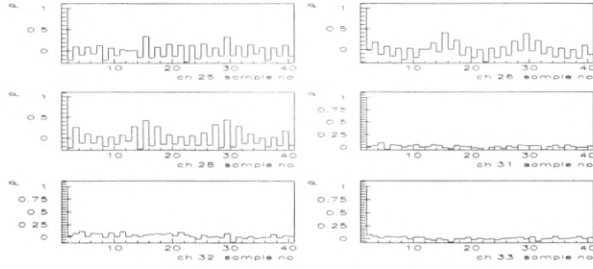


Figure 41: Sample PMT channels as in Figure 40, but for high gain.

ADCs. A detailed description of the 3-in-1 can be found in [73]. 27 PMTs were read out with 10 bit FERMI ADCs and 18 PMTs with 12 bit commercial ADCs (cells A7-A10, BC6-BC9 and D3). In total there were 90 ADC channels.

### 9.6.1 Pedestal analysis

During 1998 the same 10 bits ADCs were used as in 1996 and 1997. However, now they were connected to bigain 3-in-1s. One striking feature of the 10 bits pedestals is the presence of strong correlations, see Figure 40. The same type of strong correlations were seen in 1996 and 1997, but the correlations then were even stronger and the  $\sigma$  almost twice as large, so the 10 bits ADCs cannot alone explain the large noise in 96-97 data. The small differences between low and high gain, see Figures 40 and 41 tell us that during 98, the main correlated noise source is the 10 bits ADCs. However, as we see in the pedestal overview in Figure 42 the noise levels are very low.

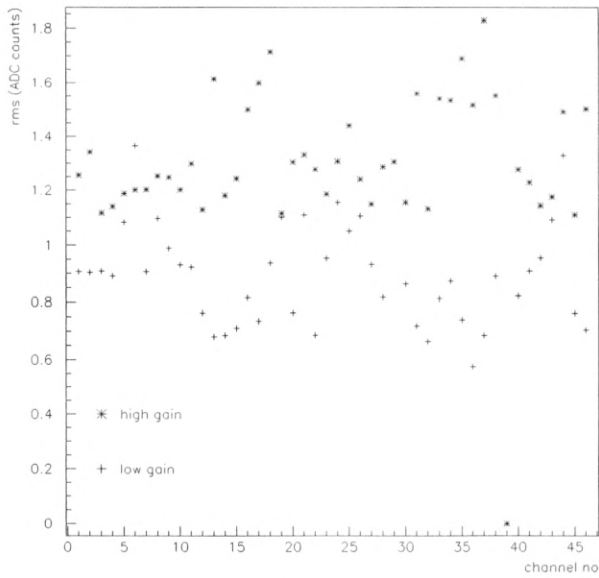


Figure 42: Overview of the pedestal RMS during 1998. Both low and gain gain channels are shown. Since the vertical scale is in ADC counts it does not reflect the physical noise levels. 12 bits ADCs have 0.007 pC/count in low gain and 0.45 pC/count in high gain. For the 10 bits ADCs the numbers are 0.014 pC/count and 0.87 pC/count. Channel 13, 16-18, 31-38 are 12 bits ADCs.

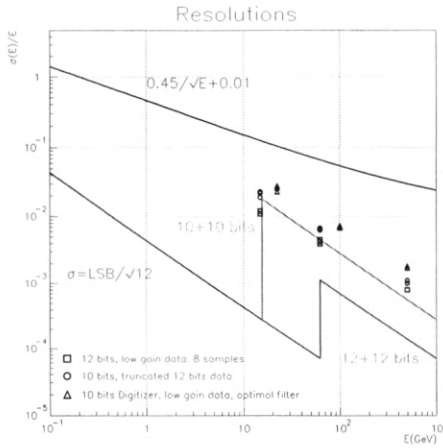


Figure 43: Resolution for a single electronics channel. The points represent charge injection data and the lines represent analytical calculations. These are compared to the intrinsic resolution of the calorimeter. Remember that for one cell in the calorimeter there are two electronics channels.

### 9.6.2 10 bits or 12 bits ADCs in the final design

One of the goals with the 1998 test-beam was to verify the performance with 10 bits ADCs. The place where the calorimeter resolution is most affected is in the low gain channel at the gain switch, see Figure 43. The figure illustrates single cell comparisons between analytical calculations, 12 bits charge injection data in 1997, 10 bits truncated from 12 bits in 1997 and results with 10 bit data taken with the new in drawer Digitizer in the end of 1998. Details concerning the 10 bits truncated data can be found in Paper V. The Digitizer data was analyzed and no severe deviations from the simulations were found, except for large low frequency noise in a few channels. The problem could easily be traced to the motherboard hardware. The margin is still good between the calorimeter and the intrinsic Digitizer resolution, remember that the two contributions are orthogonal. Electron resolution during calibration runs is not believed to be relevant for the final energy resolution since they are only used for the absolute scale calibration. One might worry if the single cell assumption really is the worst case. But any vicious energy distribution among the cells, e.g. at the gain switch, cause the resolution to scale in the same way as the calorimeter so the margin remains the same at higher energies as at the gain switching point.

During 1998 a decision was finally taken to use 10 bits ADCs for the Digitizer bigain readout.

## 10 Conclusions and outlook

The ATLAS detector and the LHC accelerator is currently, at the time of writing, in the production state and aim to be ready for data taking in 2007. There are no technical doubts that they together will fulfill the huge discovery potential expected from the physics community. In this thesis we have seen examples of extensions to the Standard Model where ATLAS and the LHC will be able to excel over previous measurements. In the search for new physics, supersymmetry together with the Higgs sector will be the main discovery targets.

However, ATLAS is a general purpose detector and will provide a wealth of precision measurements of the SM. Not only will many of the SM parameters be measured to much better precision, but probably equally important, strong bounds will be put on the deviations from the symmetries imposed by the SM. Examples of this are the triple gauge couplings which are very sensitive to beyond the SM effects. The important constraints on the non renormalizable interactions are, as we have seen in this thesis, not limited only to the pure gauge couplings. Any coupling in the SM could have an anomalous contribution that may provide a window to physics beyond the SM. These are all solid measurements that will enlarge our knowledge even in the total absence of both a Higgs sector and supersymmetry.

## Acknowledgments

First of all I would like to express my gratitude toward my supervisor Prof Kerstin Jon-And for all the support I have received during the years. It is a simple fact that without her this thesis would not have been written.

I would also like to thank the Head of the department for the Stockholm group Prof Sven-Olof Holmgren, for giving me the opportunity to do research within the area of fundamental particle physics in an environment where engagement and freedom of mind are encouraged.

I thank Dr Sten Hellman, who has also been my supervisor, for all the help and encouragement I received. He has always been able to provide the important second viewpoints in many difficult cases.

At CERN I have had the privilege to work with many outstanding physicists. Those I would like to thank in particular are Dr Martine Bosman, Dr Giacomo Polesello, Dr Ilias Efthymiopoulos, Dr Ian Hinchliffe and Dr Frank Paige.

A special thanks to Prof Per Osland for letting me work for a period of time at Bergen University and for his ability to create a stimulating environment for people to share ideas. Here I also take the opportunity to thank Wafaa Khater, Prof Pran Pandita.

I thank Anna Lipniacka and Bohdan Grzadkowski for helping me with difficult physics questions.

I thank my fellow room mates Jörgen Dalmau, Dr Lena Leinonen, Per Johansson and Patrik Ekström who have helped me with many of those problems one encounters in the day to day work.

Finally a big thanks to all the members of the Stockholm group.

## A Conventions and definitions

### A.1 Units

In high energy physics the preferred units are the natural units where

$$c = \hbar = 1$$

This is convenient since mass and energy then have the same units, and time and length become the inverse of mass and energy. In the end one needs to convert back to standard units. For example, in the cross-section calculations an useful conversion factor is

$$(1 \text{ GeV})^{-2} (\hbar c)^2 = 0.3894 \times 10^{-27} \text{ cm}^2 = 0.3894 \text{ mbarn}$$

### A.2 Special relativity

The background geometry for the fields is flat Minkowski space in which a point in space-time is specified by the 4-vector

$$x^\mu = (x^0, \vec{x}), \quad x_\mu = g_{\mu\nu} x^\nu = (x^0, -\vec{x}).$$

The 4-momentum is given by

$$p^\mu = (E, \vec{p}),$$

where  $E$  is the energy and  $\vec{p}$  is the 3-momentum. The particle rest mass ( $m$ ) is then

$$p^\mu p_\mu = E^2 - |\vec{p}|^2 = m^2.$$

The transformation from one inertial frame to another frame ('') moving with relative velocity  $\beta$  in the  $x^1$  direction is given by the Lorentz boost transformation

$$\begin{pmatrix} x^0 \\ x^1 \end{pmatrix}' = \begin{pmatrix} \cosh \eta & -\sinh \eta \\ -\sinh \eta & \cosh \eta \end{pmatrix} \begin{pmatrix} x^0 \\ x^1 \end{pmatrix}$$

where  $\eta$  defines the rapidity and  $\beta = \tanh \eta$ . In the calculations the following relations are useful

$$\begin{aligned} \beta &= \frac{p}{E} \\ \gamma &= (1 - \beta^2)^{-1/2} = \frac{E}{m} \\ \cosh \eta &= \gamma \\ \sinh \eta &= \gamma \beta \end{aligned}$$

The Lorentz transformation can be extended to all 3 spatial dimension including both boosts and rotations and forms the symmetry group  $O(3, 1)$ . In practice a very useful formula for an arbitrary boost is [74]

$$\begin{aligned} (x^0)' &= \gamma(x^0 - \vec{\beta} \cdot \vec{x}) \\ (\vec{x})' &= \vec{x} + \frac{\gamma - 1}{\beta^2}(\vec{\beta} \cdot \vec{x})\vec{\beta} - \gamma\vec{\beta}x^0 \end{aligned}$$

### A.3 The Dirac field

Spin half particles are called fermions and the associated wave function is antisymmetric under the interchange of two particles. The fermionic field is a solution to the Dirac equation

$$(i\gamma^\mu \partial_\mu - m)\psi = 0,$$

where the  $\gamma$ -matrices satisfies the Dirac algebra

$$\gamma^\mu \gamma^\nu - \gamma^\nu \gamma^\mu = 2g^{\mu\nu}.$$

This thesis uses the chiral representation for  $\gamma$ -matrices, which make the separation of left and right helicity states explicit

$$\gamma^0 = \begin{pmatrix} 0 & 1 \\ 1 & 0 \end{pmatrix}, \quad \gamma^i = \begin{pmatrix} 0 & \sigma^i \\ -\sigma^i & 0 \end{pmatrix}, \quad \gamma^5 = \begin{pmatrix} -1 & 0 \\ 0 & 1 \end{pmatrix}.$$

Pauli matrixes ( $\sigma^i$ ) are defined as

$$\sigma^1 = \begin{pmatrix} 0 & 1 \\ 1 & 0 \end{pmatrix}, \quad \sigma^2 = \begin{pmatrix} 0 & -i \\ i & 0 \end{pmatrix}, \quad \sigma^3 = \begin{pmatrix} 1 & 0 \\ 0 & -1 \end{pmatrix}.$$

Helicity is a frame dependent concept and is defined as  $h = \vec{p} \cdot \vec{s}$ , where  $\vec{s}$  is the particle spin. The projection of  $\psi$  into left and right helicity is given by the projection operators

$$P_L = \frac{1 - \gamma^5}{2}, \quad P_R = \frac{1 + \gamma^5}{2}, \quad P_L \psi = \psi_L, \quad P_R \psi = \psi_R.$$

The Dirac equation is the equation of motion given by the Lagrangian

$$\mathcal{L}_f = \bar{\psi}(i\gamma^\mu \partial_\mu - m)\psi, \quad \bar{\psi} = \psi^\dagger \gamma^0.$$

It is important to understand that bilinears, that is  $\bar{\psi}\Gamma\psi$  where  $\Gamma$  is a  $4 \times 4$  matrix, can be decomposed according to the transformation properties under the Lorentz group.  $\Gamma$  can be completely decomposed into terms in the set

$$[1, \gamma^\mu, \sigma^{\mu\nu}, \gamma^\mu \gamma^5, \gamma^5],$$

where

$$\sigma^{\mu\nu} = \frac{i}{2} [\gamma^\mu, \gamma^\nu].$$

The transformations properties are: scalar, vector, tensor, pseudo-vector and pseudo-scalar.

## A.4 Gauge connections

When the Lagrangian is demanded to be invariant under the local field symmetry transformations of the type

$$\Psi(x)' = e^{iw^a(x)T^a} \Psi(x)$$

where  $T^a$  are the generators of a Lie group one finds that the normal derivate ( $\partial_\mu$ ) cannot be used since fields with different phases are compared. The solution is to introduce a covariant derivative ( $D_\mu$ ) such that the field and the covariant derivative acting on the field have the same transformation properties. By pure geometrical arguments  $D_\mu$  is given by

$$D_\mu = \partial_\mu - igA_\mu, \quad A_\mu = A_\mu^a T^a.$$

The coupling constant  $g$  is the coupling to the connections or gauge fields  $A_\mu^a$ . The associated field strength is given by

$$-igF_{\mu\nu} = [D_\mu, D_\nu], \quad F_{\mu\nu} = F_{\mu\nu}^a T^a.$$

If the field strength is expanded an important feature of non commuting (non abelian) gauge groups is revealed

$$F_{\mu\nu} = \partial_\mu A_\nu - \partial_\nu A_\mu - ig[A_\mu, A_\nu].$$

The field strength contains a non linear part which is present only for non abelian gauge groups. The commutator is given by the generators of the Lie group, that is

$$[T^a, T^b] = if^{abc}T^c$$

where  $f^{abc}$  are the group structure constants.

For generators of the SM symmetries we choose to associate  $SU(2)$  with  $\tau^i = \frac{\sigma^i}{2}$ ,  $SU(3)$  with  $\frac{\lambda^i}{2}$  where  $\lambda^i$  are the eight Gell-Mann matrices, and  $U(1)$  with the weak hypercharge given by the Gell-Mann-Nishijima formula  $Y = Q - \tau^3$  where  $Q$  is the electric charge.

## A.5 Lie groups

A manifold, that is a continuous geometrical object, that also forms a group is called a Lie group. The generators of the group ( $T^a$ ) obey the commutator relationship

$$[T^a, T^b] = if^{abc}T^c.$$

This is called a Lie algebra where  $f^{abc}$  are the structure constants obeying the Jacobi identity

$$f^{abc}f^{bcd} + f^{bde}f^{cad} + f^{cde}f^{abd} = 0.$$

The transition from the Lie algebra to the Lie group is possible by exponentiation

$$e^{w^a T^a} \simeq 1 + w^a T^a + \mathcal{O}(w^2).$$

In the case of hermitian generators the unitarity can be made explicit by

$$e^{iw^a T^a} \simeq 1 + iw^a T^a + \mathcal{O}(w^2).$$

The symmetries of the SM are examples of groups with unitary representations of finite dimension (compact).  $U(N)$  are unitary transformations of dimension  $N$  and  $SU(N)$  are  $U(N)$  with the condition  $\det(U) = 1$ .  $SO(N)$  are orthogonal unitary transformations that preserves the symmetric inner product and  $O(N)$  is  $SO(N)$  including reflections. The Lorentz group  $O(3, 1)$  is an example of a group with no finite dimensional unitary representation. The interest in Lie groups stems from the fact that they have been classified into a very limited set. Many classes turn out to be fundamental in the description of the laws of physics.

## References

- [1] For a historical overview and pedestrian introduction see: S.F. Novaes, “Standard Model: An Introduction”, hep-ph/0001283
- [2] T. Kajita [Super-Kamiokande Collaboration], “Atmospheric neutrino results from Super-Kamiokande and Kamiokande: Evidence for nu/mu oscillations”, Nucl. Phys. Proc. Suppl. **77** (1999) 123.
- [3] G. ’t Hooft, Phys. Rev. Lett. **37** (1976) 8.
- [4] V. Baluni, Phys. Rev. D **19** (1979) 2227.
- [5] R. F. Streater, A. S. Wightman, “PCT, Spin and Statistics and all that”, Benjamin Inc., New York, 1964.
- [6] J. H. Christenson, J. W. Cronin, V. L. Fitch and R. Turlay, Phys. Rev. Lett. **13**, 138 (1964).
- [7] L. Wolfenstein, Phys. Rev. Lett. **13** (1964) 562.
- [8] B. Aubert et al. [Babar Collaboration], Phys. Rev. Lett. **87**, 091801 (2001).
- [9] K. Abe et al. [Belle Collaboration], Phys. Rev. Lett. **87**, 091802 (2001).
- [10] M. E. Peskin, D. V. Schroeder, “An introduction to Quantum Field Theory”, Addison-Wesley, 1995.
- [11] S. L. Glashow, J. Iliopoulos and L. Maiani, Phys. Rev. D **2** (1970) 1285.
- [12] M. Kobayashi, and T. Maskawa, Prog. Theor. Phys. **49** 652 (1973).
- [13] ATLAS Detector and Physics Performance TDR, CERN/LHCC/99-14.
- [14] R. Wigmans, “On the energy resolution of uranium and other hadron calorimeters”, Nucl. Instrum. Methods **A259** (1987) 389-429.
- [15] R. Wigmans, “High resolution calorimetry”, Nucl. Instrum. Methods **A265** (1988) 273-290.
- [16] C. W. Fabian and T. Ludlam, Ann. Rev. Nucl. Part. Sci. **32** (1982) 335.
- [17] E. Bernardi et al., “Performance of a compensating lead-scintillator hadronic calorimeter”, Nucl. Instrum. Methods **A262** (1987) 229-242.
- [18] F. Ariztizabal et al., “Construction and Performance of an Iron-Scintillator Hadron Calorimeter with Longitudinal Tile Configuration”, Nucl. Instrum. Methods **A349** (1994) 384.
- [19] ATLAS Tile Calorimeter TDR, CERN/LHCC/96-42.

- [20] J. Badier et al., “Test result of an electromagnetic calorimeter with 0.5 mm scintillating fibers readout”, Nucl. Instrum. Methods **A337** (1994) 314-325.
- [21] M.P.Casado and M. Cavalli-Sforza, “H1-inspired analysis of the 1994 combined test of the Liquid Argon and Tilecal calorimeter prototypes”, ATL-TILECAL-96-075 (1996).
- [22] W.E. Cleland, E.G. Stern, “Signal processing considerations for liquid ionization calorimeters in a high rate environment”, Nucl. Instr. and Methods, **A 338** (1994) 467-497.
- [23] Jim Pilcher, Private communications.
- [24] ATLAS Technical Proposal CERN/LHCC/94-43
- [25] S. Berglund et al., “A Digitizer System for the Tile Calorimeter”, CERN/ATL-TILECAL-97-132.
- [26] S. D. Drell et al., Phys. Rev. **187** 2159 (1969).
- [27] G. Hanson et al., Phys. Rev. Lett. **35** 1609 (1975).
- [28] J. E. Huth et al, Proceesings of the Summer Study on High Energy Physics, Snowmass, Colorado, 1990, p. 134.
- [29] G. Sterman and S. Weinberg, Phys. Rev. Lett. **39**, 1436 (1977)
- [30] T. Sjöstrand, Comp. Phys. Commun. **28** 227 (1983).
- [31] GEANT 3, ATLAS version 3216 98.2. DICE 3.20 geometry and digitization.
- [32] M. Seymour, Zeit. Phys. C **62** 127 (1993).
- [33] S.D. Ellis and D.E. Soper, Phys. Rev. D **48** 2160 (1993).
- [34] T Akers et al., OPAL Collaboration, Zeit. Phys. C **63** 197 (1994).
- [35] ATLAS Calorimeter performance, CERN/LHCC/96-40.
- [36] A. Bilal, arXiv:hep-th/0101055.
- [37] L. Haag, J. Lopuszanski and M. Sohnius, Nucl. Phys. B **88**, 257 (1975).
- [38] S. Dimopoulos, H. Georgi, Nucl. Phys. B **193**, 150 (1981).
- [39] R. N. Mohapatra, “Supersymmetric Grand Unification: Un update”, hep-ph/9911272.
- [40] H.P. Nilles, Phys. Rep. **110**, 1 (1984).
- [41] M. Dine, W. Fishler, Phys. Lett. D **110**, 227 (1982).

- [42] M. Dine, A. E. Nelson, Phys. Rev. D **48**, 1277 (1993).
- [43] G.F. Giudice, R. Rattazzi, Theories with Gauge-Mediated Supersymmetry Breaking, hep-ph/9801271.
- [44] M. Krämer, “Supersymmetric particle production at hadron colliders”, hep-ph/9809259.
- [45] B. C. Allanach, C. G. Lester, M. A. Parker and B. R. Webber, JHEP **0009** (2000) 004.
- [46] I. Hinchliffe and F. E. Paige, “Measurements in gauge mediated SUSY breaking models at LHC,” Phys. Rev. D **60** (1999) 095002.
- [47] F. Paige, S. Protopopescu, “ISAJET 7.44 A Monte Carlo Generator for  $p\bar{p}$ ,  $\bar{p}p$  and  $e^+e^-$  Reactions”, <http://penguin.phy.bnl.gov/~paige/>
- [48] G. Polesello, A. Rimoldi, “Reconstruction of quasi-stable charged sleptons in the ATLAS Muon Spectrometer”, ATL-MUON-99-006 (1999).
- [49] T. Sjöstrand, PYTHIA 5.7 and JETSET 7.4, Computer Physics Common. **82**, 1994.
- [50] E. Richter-Was, D. Froidevaux, L. Poggiali, “A Fast Simulation Package for ATLAS”, ATL-PHYS-98-131 (1998).
- [51] B. Grzadkowski and W. Y. Keung, Phys. Lett. B **319** (1993) 526.
- [52] A. G. Cohen, D. B. Kaplan and A. E. Nelson, Ann. Rev. Nucl. Part. Sci. **43** (1993) 27.
- [53] S. Bar-Shalom, D. Atwood and A. Soni, Phys. Rev. D **57** 1495 (1998).
- [54] Jin Min Yang and Bing-Lin Young, Phys. Rev. D **56** (1997) 467.
- [55] Jin Min Yang and Bing-Lin Young, Phys. Rev. D **56** (1997) 5907.
- [56] P. Haberl, O. Nachtmann and A. Wilch, Phys. Rev. D **53** (1996) 4875.
- [57] G. J. Gounaris, D. T. Papadamou and F. M. Renard, Z. Phys. C **76** (1997) 333
- [58] R. Bonciani et al, “NLL Resummation of the Heavy-Quark Hadroproduction Cross-Section”, hep-ph/9801375.
- [59] H. L. Lai et al., Phys. Rev. D **51** (1995) 4763
- [60] D. Atwood, A. Aeppli and A. Soni, Phys. Rev. Lett. **69** (1992) 2754.
- [61] Phys. Rev. D **58** (1998) 114002.
- [62] A. Soni and R. M. Xu, Phys. Rev. Lett. **69** (1992) 33.

- [63] B. Grzadkowski, Talk at the Fourth Nordic LHC Physics Workshop, Stockholm 22-24 November 2001.
- [64] TileMon user manual, [http://atlasinfo.cern.ch  
/Atlas/SUB\\_DETECTORS/TILE/testbeam/tb1999/TestBeam\\_1999run](http://atlasinfo.cern.ch/Atlas/SUB_DETECTORS/TILE/testbeam/tb1999/TestBeam_1999run)
- [65] ZEBRA, CERN Program Library Long Writeups Q100/Q101.
- [66] FERMI collaboration, a digital Front End and Readout MIcroSystem for high resolution calorimetry, CERN/ATL-DAQ-94-015.
- [67] FERMI collaboration, “Results of the testbeams of RD16 (FERMI) With electromagnetic and hadronic calorimeter prototypes”, CERN/ATL-DAQ-95-042.
- [68] S. Angvall et al., “Evaluation of Fermi Readout of the ATLAS Tilecal Prototype”, CERN/ATL-TILECAL-97-116.
- [69] Svante Berglund, Private communications.
- [70] C. W. Cattaneo, “A technique for signal shape reconstruction in sampled systems”, FERMI note # 45, Submitted to Signal Processing.
- [71] T. Davidek and R. Leitner, “Parametrization of the Muon Response in the Tile Calorimeter”, ATL-TILECAL-97-114.
- [72] I. Efthymiopoulos and T. Kontos, “Analysis of the CIS calibration data of the new Tile Calorimeter bi-gain readout system”, ATLAS internal note, TILECAL-NO-143.
- [73] K. Andersson et al., “Front-end Electronics for the ATLAS Tile Calorimeter”, Writeup from 1998 Rome LEB meeting.
- [74] J. D. Jackson, Classical Electrodynamics, John Wiley and Sons Inc.
- [75] D.E. Groom et al., The European Physical Journal C **15** (2000).





